Assimilation of GOES-R Geostationary Lightning Mapper Flash Extent Density in JEDI LETKF, LGETKF, and En3DVar: Development of Assimilation Capabilities and Test with a Convective Storm Case over the United States

RONG KONG,[a] MING XUE,[a,b] CHENGSI LIU,[a] JUN PARK,[a] AMANDA BACK,[c,d] AND EDWARD R. MANSELL[e]

[a] *Center for Analysis and Prediction of Storms, Norman, Oklahoma*
[b] *School of Meteorology, University of Oklahoma, Norman, Oklahoma*
[c] *Cooperative Institute for Research in the Atmosphere, Colorado State University, Fort Collins, Colorado*
[d] *NOAA/Global Systems Laboratory, Boulder, Colorado*
[e] *NOAA/National Severe Storms Laboratory, Norman, Oklahoma*

(Manuscript received 6 January 2025, in final form 22 September 2025, accepted 8 October 2025)

ABSTRACT: In this study, we implement the capabilities to assimilate GOES-R Geostationary Lightning Mapper flash extent density (FED) data within the Joint Effort for Data Assimilation Integration (JEDI) system, coupled with the Finite-Volume Cubed-Sphere (FV3) dynamical core for forecasting. We evaluate different data assimilation (DA) methods, including the local ensemble transform Kalman filter (LETKF), gain-form LETKF (LGETKF), and ensemble 3DVAR (En3DVar), for a test case with active convection over the United States. The convergence behavior of En3DVar is consistent with expectations. Sensitivity to the vertical localization strategies in the algorithms is examined. LGETKF applies gain-form vertical localization, which demands more computational resources than LETKF and En3DVar when using smaller vertical localization radii [e.g., 0.2 or 0.4, compared to larger radii like 1 or 4 in $\ln(p/p_0)$ space]. While En3DVar achieves a better balance between accuracy and efficiency, it demands significantly more memory than LETKF and LGETKF, with the current JEDI implementation at least. Sensitivity experiments indicate that larger vertical localization radii [e.g., 4 in $\ln(p/p_0)$ space] improve analysis and 6-h forecast after DA when verified against the observed reflectivity field. Overall, all three DA methods produce comparable results, outperforming the experiment that does not assimilate any data. This work serves to establish the credibility of the lightning DA implementation within the new JEDI system and to understand the effects of algorithm differences related to vertical covariance localization on the assimilation of FED data, whose observation operator involves column integration of a hydrometeor state variable.

SIGNIFICANCE STATEMENT: This work implemented capabilities to assimilate high-frequency lightning mapper data from the GOES-R geostationary weather satellites, within the next-generation data assimilation system called the Joint Effort for Data assimilation Integration, which will be used by all operational weather prediction systems of the U.S. National Weather Service. A lightning flash extent density (FED) observation operator with its tangent linear and adjoint components was implemented in the Joint Effort for Data Assimilation Integration's (JEDI's) Unified Forward Operator, making FED assimilation available to both ensemble Kalman filter and variational algorithms within JEDI. The new capability is tested with three data assimilation algorithms: the local ensemble transform Kalman filter (LETKF), gain-form LETKF, and ensemble 3DVAR to verify correctness across the algorithms and examine their different vertical localization treatments. Using a convective storm case, we confirm the correctness of the implementation and demonstrate potential positive impacts of assimilating the lightning data on convective storm forecasts, while noting that further multicase studies are needed to generalize the findings.

KEYWORDS: Satellite observations; Ensembles; Short-range prediction; Data assimilation; Numerical analysis/modeling

1. Introduction

The accuracy of initial conditions is crucial for improving the precision of numerical weather prediction (NWP) (Kalnay 2002). A lack of convective-scale information in the initial conditions leads to the well-known spinup issue in precipitation forecasting (Sun and Crook 1997; Xue et al. 2003; Zhang et al. 2004; Kain et al. 2008; Bauer et al. 2015). With the advancements in observation systems, including weather radars and satellites, it is possible to capture fine convective-scale details typically associated with precipitation systems within the NWP initial conditions. Previous studies have consistently demonstrated the value of radar data assimilation (DA) in improving short-term weather forecasts (Tong and Xue 2005; Hu et al. 2006a,b; Jung et al. 2008; Aksoy et al. 2009, 2010; Gao and Stensrud 2012; Sun and Wang 2013; Kong et al. 2018; Liu et al. 2019, 2020; Kong et al. 2021). Other studies have also demonstrated the importance of high-resolution satellite data in improving storm-scale NWP (Zhang et al. 2016a; Honda et al. 2018; Jones et al. 2018; Minamide and Zhang 2018; Zhang et al. 2018; Sawada et al. 2019; Jones et al. 2020; Zhu et al. 2023).

Kong's and Park's current affiliation: MMM-NCAR, 3450 Mitchell Lane Boulder, Colorado.

Corresponding author: Ming Xue, mxue@ou.edu

DOI: 10.1175/MWR-D-25-0003.1

The assimilation of observations on lightning flashes of thunderstorms or lightning data has also shown promise in improving convective storm prediction, given that the data also contain information about convection. This is particularly valuable in regions lacking ground-based weather radar coverage, where lightning data can serve as a complementary observational source. Earlier research has predominantly focused on indirect assimilation methods, employing data from various sources, including ground-based lightning observation networks and pseudo–Geostationary Satellite Lightning Mappers (GLMs) lightning observations prior to the availability of real-time GLM data. These lightning data have been used in different ways: either to adjust latent heat or humidity profiles within the model (Alexander et al. 1999; Chang et al. 2001; Papadopoulos et al. 2005; Mansell et al. 2007) or to be converted into pseudo-observations of moisture, temperature, reflectivity, or vertical velocity that are then assimilated (Fierro et al. 2012, 2014; Marchand and Fuelberg 2014; Fierro et al. 2015, 2016, 2019; Ge et al. 2019; Hu et al. 2020; Xiao et al. 2021). These studies generally achieved positive impacts of lightning DA, and sometimes the impacts can be on par with those of radar data (Fierro et al. 2016). It is worth noting, however, that most of these methods are indirect assimilation methods that rely on some form of derived pseudo-observations, and the analysis approach is generally univariate, with Xiao et al. (2021) being an exception. Thus, they do not update multiple model state variables consistently; the latter is expected to further increase the positive impacts.

The development of ensemble-based DA methods, including the ensemble Kalman filter (EnKF; Evensen 1994) and ensemble-variational (EnVar) methods (Hamill and Snyder 2000; Lorenc 2003), and their applications to convective-scale DA with radar data (Snyder and Zhang 2003; Tong and Xue 2005; Kong et al. 2018) have prompted their application to directly assimilate lightning data. Incorporating flow-dependent ensemble background error covariance within such systems has enabled the simultaneous updating of all model state variables. At the same time, the direct use of observation operators removes the need for prior retrieval or conversion of state variables that are often empirical. For instance, Mansell (2014) and Allen et al. (2016) employed the EnKF method to assimilate simulated or pseudo–flash extent density (FED) observations into a cloud model. In our recent research, we have developed direct assimilation capabilities for real GLM FED data with the EnKF and EnVar DA algorithms within the Gridpoint Statistical Interpolation analysis system (GSI; Kleist et al. 2009) framework. Preliminary case studies have shown improvement in the analysis and short-term forecast of convective storms (Kong et al. 2020, 2022, 2024).

In this study, we implement and test the GOES-R lightning DA capabilities within the new Joint Effort in Data Assimilation Integration (JEDI; https://www.jcsda.org/jcsda-project-jedi). JEDI is being developed to replace the existing GSI DA system for all National Weather Service (NWS) operational forecast systems. It offers a modular architecture that supports both variational and ensemble DA algorithms, with recently implemented capabilities for assimilating microwave radiance and radar data (Liu et al. 2022; Park et al. 2023). As part of this study, we migrated the FED observation operator previously developed for GSI into the Unified Forward Operator (UFO) module of JEDI. This operator follows the nonlinear formulation introduced in Kong et al. (2022), which uses a third-order polynomial fit between model graupel mass and observed FED. The implementation includes the forward operator as well as its tangent linear and adjoint components, enabling its use in both ensemble Kalman filter and variational DA algorithms in JEDI. The core operator routines are written in FORTRAN and remain largely similar to the GSI implementation. Only minor modifications were required to interface with JEDI's higher-level C++ infrastructure, primarily through standard FORTRAN–C interoperability wrappers provided by the UFO framework. This capability represents the first GLM FED operator implemented in the JEDI system, and it has been publicly released as part of the JEDI community codebase. The JEDI DA system is coupled with the Finite-Volume Cubed-Sphere (FV3) forecast model (Lin 2004; Putman and Lin 2007; Harris et al. 2021).

Specifically, this paper details the implementation and testing of GLM FED DA capabilities using the local ensemble transform Kalman filter (LETKF; Hunt et al. 2007), the local gain-form ensemble transform Kalman filter (ETKF) (LGETKF; Bishop et al. 2017; Lei et al. 2018), and ensemble 3DVAR (En3DVar) algorithms within JEDI. The primary objective is to validate the implementation of these new capabilities and to understand and document their behaviors and performance in assimilating GLM FED data, whose observation operator is atypical. While comparing the relative performance of these well-established algorithms in general is not the primary purpose, we focus on examining the particular behaviors of each algorithm most relevant to FED data.

The paper is structured as follows: Section 2 outlines the DA methods and procedures utilized in the study. Section 3 describes the simulation setup and experimental design. Section 4 focuses on the algorithm behaviors, including single-observation experiments that clarify the behaviors of observation-based and model-space localization used by different algorithms. It first examines the convergence of cost function minimization in En3DVar to validate the variational implementation. It also presents sensitivity tests varying vertical localization radii and identifies the optimal vertical localization radius based on the fractions skill score (FSS; Roberts and Lean 2008) from 6-h reflectivity forecasts following 1-h cycled DA. Section 5 presents the overall evaluation results of the DA and forecast experiments, comparing the effectiveness of different assimilation approaches using objective skill scores. Finally, section 6 summarizes the findings and conclusions from the study.

2. Assimilation methods and procedures

Prior literature has described the formulations of LETKF, LGETKF, and En3DVar. In this section, we briefly describe these algorithms with emphasis on how covariance localization is treated in each algorithm. The En3DVar algorithm implemented in JEDI employs a specialized package for representing and localizing ensemble background error

covariance on unstructured grids, which will also be briefly described.

a. The LETKF algorithm with R-based localization

The LETKF (Hunt et al. 2007) is a variant of EnKF and is a localized version of the ETKF (Bishop et al. 2001). In LETKF, observations are divided into local patches, each centered on a specific grid point. The algorithm draws on the concept of the local ensemble Kalman filter (LEKF; Ott et al. 2004), particularly in its approach of updating the central grid point of each patch in parallel to optimize computational efficiency (Miyoshi and Yamane 2007; Liu et al. 2008). The LETKF employs observation-based localization, where the observation error variance R is increased with distance from the grid point to achieve the effect of background error covariance localization (Hunt et al. 2007; Miyoshi and Yamane 2007; Greybush et al. 2011). The method is often referred to as observation-/R-based localization (Nerger et al. 2012).

b. The LGETKF algorithm with R-based and model-space localizations

The LGETKF, based on Bishop et al. (2017) and Lei et al. (2018), offers a model-space covariance localization that does not require the knowledge of the physical location of the observation assimilated. This is especially suitable for satellite radiance observations and for the GLM lightning FED data, whose observation operators involve vertical integration and the observations themselves are not defined at particular height levels. The idea of leveraging empirical orthogonal function (EOF) decomposition (Lorenz 1956) for model-space localization is also utilized by Liu et al. (2009) for a 4DEnVar algorithm. In LGETKF, the concept of retained covariance and the number of eigenvectors plays a significant role in the localization performance. The retained covariance in LGETKF refers to the portion of the covariance matrix preserved during the localization and transformation processes. Selecting an appropriate number of eigenvectors is critical for balancing computational cost and the degree of covariance approximation. Retaining too few eigenvectors and the associated covariance can result in loss of essential information, degrading the filter's ability to accurately represent system state and uncertainties. Conversely, retaining too many eigenvectors can increase computational costs without significantly improving accuracy. Therefore, choosing the right number of eigenvectors and retaining the right amount of covariance are important for balancing LGETKF DA performance and efficiency. In this study, we use the LGETKF solver as implemented in JEDI, which applies model-space localization in the vertical direction using the gain formulation, while retaining the observation-space localization in the horizontal directions using R-based localization with the Gaspari–Cohn function. This follows the standard LGETKF implementation structure established in GSI and adopted in JEDI. To ensure compatibility with our previous GLM FED assimilation work in the GSI framework (e.g., Kong et al. 2020, 2024), we use the GSI-based FORTRAN implementations of both LETKF and LGETKF within the JEDI system. This choice also facilitates verification of the FED observation operator and provides a consistent basis for comparing across different DA algorithms. In JEDI, another version of LETKF implemented in C++ is also available.

c. The En3DVar algorithm with BUMP-based localization

The En3DVar algorithm used in this study follows the hybrid-EnVar formulation originally proposed by Hamill and Snyder (2000), in which the background error covariance matrix $\mathbf{B}$ is constructed as a weighted sum of a static component $\mathbf{B}_s$ and an ensemble-based component $\mathbf{B}_e$. In our implementation, however, we use pure En3DVar (PEn3DVar) by omitting the static term (i.e., $\mathbf{B} = \mathbf{B}_e$), to ensure a fair comparison with LETKF and LGETKF, which also use only ensemble covariance.

Vertical and horizontal localization for the ensemble-based $\mathbf{B}_e$ is performed using the Background Error on an Unstructured Mesh Package (BUMP; Ménétrier 2020), a modular component of JEDI. BUMP models localization functions directly on the FV3-LAM's cube-sphere grid, offering improved flexibility and computational efficiency, especially for unstructured or limited-area domains. More specifically, localization is modeled using the normalized interpolated convolution from an adaptive subgrid (NICAS) method within BUMP, which computes correlation functions on a subset of sampling points and interpolates them to the full cube-sphere grid. Once generated, the localization matrix can be reused for subsequent DA cycles, eliminating the need to reinitialize localization each time, as is required in some recursive filter approaches.

This study builds on previous lightning DA work in GSI (Kong et al. 2020, 2022, 2024) but uses the JEDI implementation of PEn3DVar with BUMP for the first time. The use of PEn3DVar allows us to test vertical localization in model space, in a configuration consistent with LGETKF, and to better understand algorithmic behavior in response to vertically integrated lightning observations.

As in Kong et al. (2024), we will not include any static background error covariance in our tests with En3DVar in this paper, so that the algorithm is a pure En3DVar (PEn3DVar) instead of a hybrid En3DVar. Again, the main objective of this paper is not to compare different DA algorithms in general but to validate the correctness of algorithm implementations for lightning DA and to better understand the algorithm behaviors for our application. Not including static background error covariance in the En3DVar makes it more similar to the LETKF algorithms, which do not include static covariance either.

3. Simulation setup and experimental design

a. GOES-R GLM FED data processing

In this work, FED data are derived from level-II GLM lightning flash data featuring 20-s refresh rates. The dataset offers a pixel resolution of roughly 8 km over the contiguous United States (CONUS), as described in Goodman et al. (2013).

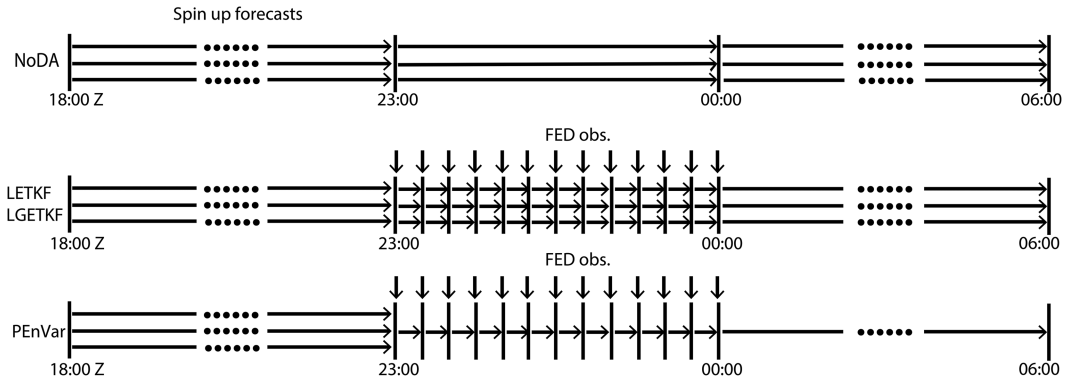

FIG. 1. Flow diagram of the (middle) LETKF and LGETKF and (bottom) PEn3DVar DA experiments vs (top) the control run. The process begins with spinup forecasts of 40 members from 2100 to 2300 UTC, starting from GDAS analyses at 1800 UTC. FED observations are assimilated in 5-min cycles between 2300 and 0000 UTC. Post-DA, ensemble forecasts for LETKF and LGETKF commence from the final analyses at 0000 UTC and continue until 0600 UTC. In the PEn3DVar experiment, a singular forecast is produced from the final analysis. The CTRL experiment, without DA, carries on with ensemble forecasts from 1800 UTC straight through 0600 UTC the next day.

To facilitate FED processing, the GLM lightning data are collected into a designated 10×10 km^2 grid. Our processing methodology aligns with the work of Bruning et al. (2019). It also involves converting the GLM data into HDF5 format, which is JEDI's official observation format.

b. *Forecast model setup and initialization of ensembles*

The FV3-LAM is used as our forecast model (Lin 2004; Putman and Lin 2007; Harris et al. 2021). FV3-LAM is used in the planned version 1 of the Rapid Refresh Forecast System (RRFSv1; Dowell et al. 2022; James et al. 2022). For our experimental setup, we closely follow the model configuration used by Park et al. (2023), which focuses on testing radar DA capabilities implemented in JEDI. Specifically, we employ a smaller domain with the extended Schmidt gnomonic projection, encompassing 310×310 horizontal grid points across Texas and Oklahoma (Fig. 1). The grid has an approximate 3-km grid spacing and 64 vertical levels. An experimental physics suite for RRFSv1 labeled "RRFS_v1_alpha" (Banos et al. 2022) is used, which includes the Thompson microphysics (Thompson et al. 2008), MYNN PBL (Nakanishi and Niino 2009; Olson et al. 2019), Noah-MP land surface (Ek et al. 2003; Niu et al. 2011), and RRTMG radiation (Mlawer et al. 1997) schemes sourced from the Common Community Physics Packages (CCPP; Heinzeller et al. 2023). The same physics suite was also used in Tong et al. (2024).

The initial ensemble is derived from the NCEP operational Global Data Assimilation System (GDAS; Derber et al. 1991; Whitaker et al. 2008; Kleist et al. 2009) EnKF analyses at 1800 UTC 20 May 2019. For lateral boundary conditions, the GDAS 3-hourly ensemble forecasts up to 9 h are employed.

c. *Design of data assimilation experiments*

Using the graupel-mass-based nonlinear GLM FED observation operator introduced by Kong et al. (2022), a series of experiments are conducted to test and validate the assimilation of FED data within the JEDI framework using three different algorithms (Table 1). Specifically, the operator is constructed from a third-order polynomial fit between the observed GLM FED and model-simulated graupel mass over a 15×15 km^2 column, as described in Kong et al. (2022). This nonlinear formulation accounts for the complex relationship between lightning activity and graupel distribution. In Kong et al. (2022), it was shown through experiments that this

TABLE 1. Descriptions of the DA experiments.

Experiment	Algorithm for LDA	Vertical localization radius [in $\ln(p/p_0)$ space]
NoDA	Not applicable	—
LETKF	LETKF	0.2, 0.4, 1, 4
LGETKF30%P_b	LGETKF (30% retained P_b)	0.2, 0.4, 1, 4
LGETKF60%P_b	LGETKF (60% retained P_b)	0.2, 0.4, 1, 4
LGETKF90%P_b	LGETKF (90% retained P_b)	0.2, 0.4, 1, 4
PEn3DVar	Pure En3DVar using 100% ensemble covariance, one-way coupled with LETKF with the corresponding vertical localization radii	0.2, 0.4, 1, 4
PEn3DVarG	Pure En3DVar using 100% ensemble covariance, one-way coupled with LGETKF60%P_b with the corresponding localization radii	0.2, 0.4, 1, 4

nonlinear operator yields more accurate FED forecasts than linear formulations.

The experiments focus on evaluating the impact of vertical localization radius in $\ln(p/p_0)$ space (where p and p_0 are the pressure and reference/surface pressure in hPa) and exploring the effect of retained fraction of ensemble background error covariance (P_b) in LGETKF. A control experiment, CTRL, without DA (NoDA) serves as a baseline for comparison, while experiments PEn3DVar and PEn3DVarG couple the PEn3DVar method with LETKF and LGETKF, respectively.

Table 1 provides a description of the DA experiments. The LETKF and LGETKF algorithms were tested with different vertical localization radii [0.2, 0.4, 1, and 4 in $\ln(p/p_0)$ space], while LGETKF experiments were further evaluated for varying fractions of retained P_b (30%, 60%, and 90%). The PEn3DVar experiments use 100% ensemble covariance and are one-way coupled with either LETKF or LGETKF (referred to as PEn3DVar and PEn3DVarG, respectively). Ensemble forecasts with 40 members are spun up from 1800 to 2300 UTC from GDAS analyses, after which FED observations are assimilated at 5-min intervals between 2300 and 0000 UTC (Fig. 1). Postassimilation, ensemble forecasts from LETKF or LGETKF are initialized at 0000 UTC and run until 0600 UTC. For the PEn3DVar experiments, a single deterministic forecast is produced from the final PEn3DVar analysis for the same period. The control experiment (NoDA) runs ensemble forecasts from 1800 to 0600 UTC the next day without DA.

To mitigate the development of spurious storms in the background, zero FED observations are also assimilated. This strategy follows prior work (e.g., Kong et al. 2020, 2024) and is analogous to the assimilation of zero radar reflectivity to suppress false convection (Tong and Xue 2005). This approach is supported by Mansell et al. (2002), who showed that lightning-free regions are typically associated with weak graupel loading and weak updrafts and can thus be used to constrain deep convection in numerical simulations.

An adaptive inflation factor of 0.95, which relaxes the posterior spread toward the prior spread (Whitaker and Hamill 2012; Kotsuki et al. 2017; Maldonado et al. 2020), is employed to maintain the ensemble spread. The FED operator is a vertical integral of graupel mass, which, like GLM FED observations, lacks inherent vertical location information. For LETKF, the FED observations are assumed to be at a height of 6.5 km (Allen et al. 2016; Kong et al. 2020), within the mixed-phase region where most lightning occurs. The specification of vertical location is not required for LGETKF and En3DVar, which employ model-space localization. Horizontal localization is applied with a cutoff radius of 15 km, and a small observation error of 0.5 flashes per minute per pixel is used, following Kong et al. (2020).

In all data assimilation experiments in this study, the model state vector that is updated by the DA algorithms includes not only the hydrometeor mixing ratios (graupel, snow, and rain) but also wind components (u, v, w), temperature, and water vapor mixing ratio. Although the FED observation operator is directly dependent on graupel mixing ratio only, the assimilation updates other state variables through ensemble-derived flow-dependent background error cross covariances. The indirect impacts on wind, temperature, and humidity fields have been extensively analyzed in our previous paper (Kong et al. 2020; see especially Figs. 8 and 9) and are not repeated here. This study presents the hydrometeor increments as the most immediate and interpretable response to FED observations.

d. Case overview

On 20 May 2019, the Southern Great Plains, extending to Missouri and Arkansas, experienced a notable episode of intense convective storms. These storms were driven by an upper-level trough over the eastern United States and a surface low pressure system in the central region, leading to the formation of tornadic supercells, particularly east of a pronounced dryline stretching from Texas to Missouri. The interactions of regional topography, combined with warm and moist air advection from the south and the influence of the upper-level jet stream, contributed to the development of these severe storms. As a result, the National Weather Service Storm Prediction Center issued numerous severe weather advisories. This day was marked by the occurrence of 34 tornadoes and numerous reports of wind and hail disturbances, underlining its significance in severe weather events (Fig. 2). This same case was utilized to assess the impact of radar data assimilation within the JEDI framework, using the LETKF and LGETKF algorithms as in Park et al. (2023).

To provide additional context for this case, the spatial structure and temporal evolution of the convective system are illustrated later using hourly accumulated precipitation forecasts (see Fig. 12).

4. Implementation validation and optimization of selected parameters

a. Convergence of En3DVar cost function

Since the primary focus of this study has been the implementation of lightning DA (LDA) capability within the JEDI DA framework, validating the correctness of this implementation is crucial. Variational DA requires the development of tangent linear and adjoint codes for the specified operators. Although these codes have passed tangent linear and adjoint tests in JEDI, it is essential to examine the convergence of the cost function for En3DVar.

As in many variational data assimilation systems (Courtier et al. 1994), En3DVar employs a double-loop procedure, where nonlinear observation operators are linearized within the outer loops, while cost function minimization occurs through inner-loop iterations. With the linearized observation operators, the cost function becomes quadratic and has a single minimum. During successive outer loops, linearization is performed around the updated analysis states, helping reduce approximation errors and improving the final analysis accuracy. Since the FED observation operator used in this study is nonlinear, this outer-loop mechanism is particularly important

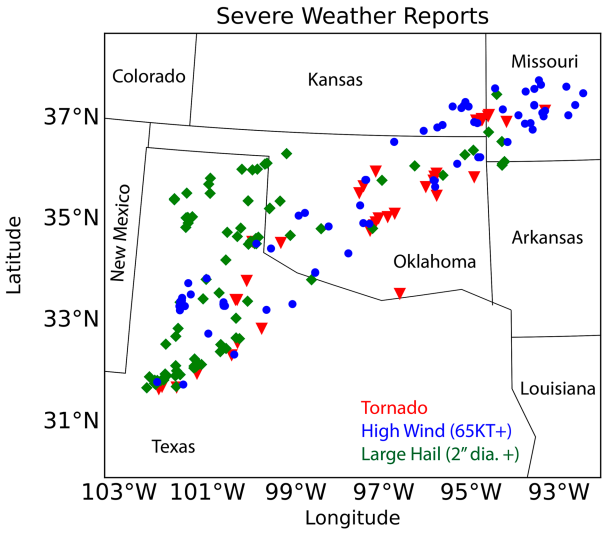

FIG. 2. Spatial distribution of severe weather events, 20 May 2019. This map highlights the geographic distribution of tornadoes, hail, and wind reports on the specified date. Tornadoes are denoted by red triangles, hail by green diamonds, and wind events by blue circles. The map includes state and country boundaries to offer geographical context and outlines the domain size of the experiment.

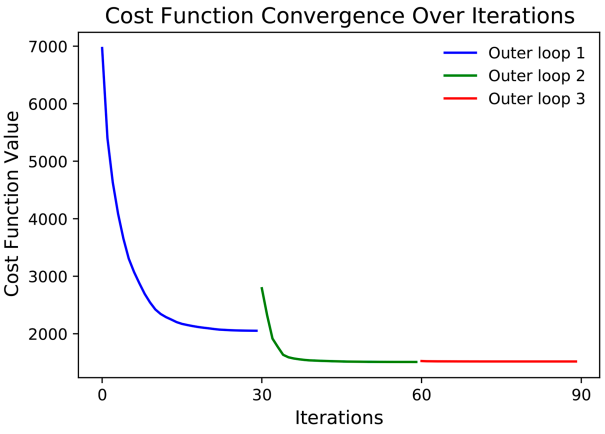

FIG. 3. Convergence of the cost function over 30 iterations for each of the three outer loops. The cost function values are plotted for each iteration within the three outer loops, labeled as outer-loop 1 (blue), outer-loop 2 (green), and outer-loop 3 (red). The horizontal axis represents the number of iterations, and the vertical axis represents the cost function value.

for obtaining consistent minimization results. Evaluating the convergence of the cost function under this outer-loop structure is essential for verifying the effectiveness of the LDA implementation and identifying the required number of outer loops and inner-loop iterations. Figure 3 illustrates the convergence of the cost function across three distinct outer-loop iterations, with each outer loop consisting of 30 inner-loop iterations, totaling 90 iterations displayed on the horizontal axis. During "outer-loop 1," there is a significant reduction in the cost function, indicating rapid convergence. In "outer-loop 2," a noticeable reduction in the cost function is also observed at the beginning, though the rate of change diminishes progressively. Conversely, "outer-loop 3" exhibits only minimal changes after the initial iterations. This pattern suggests that convergence is achieved after the first two outer loops, with subsequent iterations in outer-loop 3 contributing little to further reduction of the cost function. Therefore, two outer loops are sufficient to achieve convergence, while 30 iterations in each outer loop appear sufficient.

b. *Comparisons of computational costs among LETKF, LGETKF, and En3DVar*

In evaluating the performance of various DA algorithms, it is of practical interest to assess their computational costs and memory usage to understand their efficiency and scalability. The same number of computing nodes (5) and cores (225) are utilized across all experiments for the comparison of LDA among LETKF, LGETKF, and PEn3DVar. The percentage of retained P_b significantly influences the number of eigenvectors to be used, affecting computational cost. As shown in Table 1, we test varying levels of P_b retention in LGETKF to examine their effects on computational cost and memory usage. We explore different vertical localization radii since they also significantly influence the computational cost.

Figure 4a shows that the vertical localization radius directly affects computational costs. LETKF is consistently less expensive than LGETKF across various localization radii. The differences in computational costs between LETKF and PEn3DVar are less pronounced. For PEn3DVar, the wall-clock time shows little sensitivity to the localization radius. In the JEDI version used for this study (v1.1), the number of NICAS sampling points was fixed at 1400 (controlled by the parameter nc1max), so the computational cost is dominated by constructing and applying the covariance from these sampling points rather than by the choice of localization radius. Because the FV3-LAM domain used in this case study is relatively limited in size, 1400 sampling points provided a reasonable balance between accuracy and efficiency. In more recent JEDI/SABER versions, the parameter nc1max has been replaced by sampling and nicas.resolution options, but the principle remains the same: The computational cost depends primarily on the number of sampling points rather than the localization radius. Notably, memory usage differences become particularly significant with LGETKF, where a smaller vertical localization radius substantially increases computational cost. Higher percentages of retained background error covariance (P_b) in LGETKF are also associated with increased computational costs. This is due to the need to retain a larger number of eigenvectors to capture the covariances accurately. In contrast, LETKF shows similar computational costs across various localization radii. This is largely due to the smaller number of FED observations used in the study (9801), which reduces the impact of changes in the localization radius. When the localization radius is large (e.g., 4), the differences in computational costs between LETKF and LGETKF narrow, as there is effectively no localization in

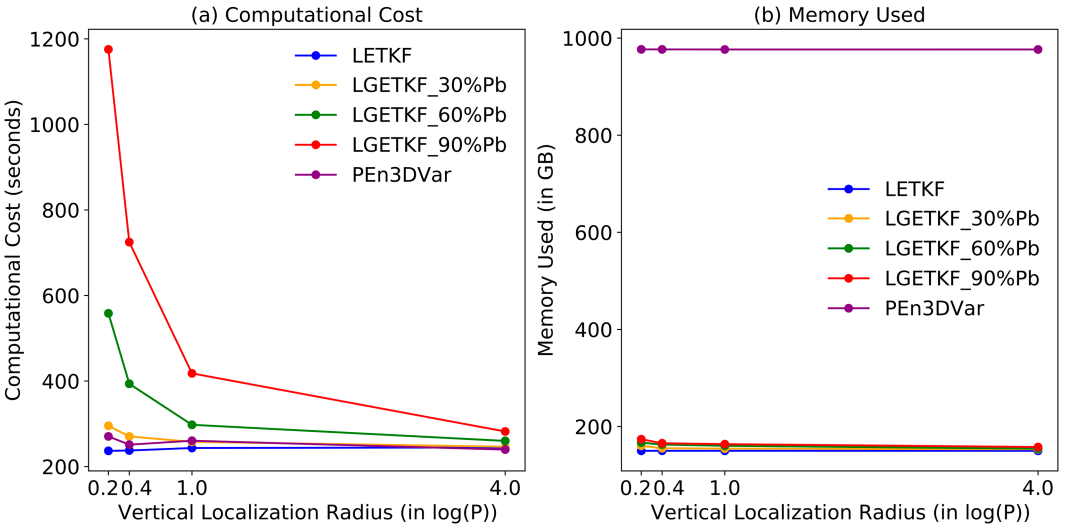

FIG. 4. Comparison of computational costs of DA methods based on vertical localization radius. (a) The computational costs in seconds (wall-clock time) for various methods against different vertical localization radii. (b) Memory usage in gigabytes for the same set of methods.

either method with such a large localization radius. However, as the localization radius decreases, the computational cost disparity increases significantly, with LGETKF becoming substantially more expensive. For FED data whose observational operator involves column integral of graupel mass, larger vertical localization radii are usually desirable (see section 4b).

Memory usage is also a critical consideration, as shown in Fig. 4b. In the JEDI version used here (v1.1), LETKF and LGETKF employed a halo-style observation distribution, while PEn3DVar used the default round-robin distribution for distributed memory processing on processor cores. This difference in distribution strategy accounts for part of the memory contrast observed in Fig. 4. PEn3DVar nevertheless demonstrates notably higher memory demands compared to LETKF and LGETKF, mainly reflecting the algorithmic requirements of the variational solver (e.g., storing and applying global covariance structures and gradients), as well as implementation details that may require further optimization, rather than the observation distribution strategy itself. This difference is observed consistently across the experiments, with memory requirements of PEn3DVar being about an order of magnitude higher (Fig. 4b). In more recent JEDI/SABER versions, the distribution must be explicitly specified in the YAML configuration, with halo typically used for ensemble Kalman filter methods and round-robin for variational methods and HofX applications.

c. *Single-observation experiments for LETKF, LGETKF, and En3DVar*

As discussed in section 2, LETKF employs R-based localization in all three dimensions, while LGETKF and En3DVar utilize model-space localization in the vertical direction. For the FED observation operator, which involves vertical integration, the behaviors of the vertical localization methods with different localization radii, especially those in model space, are unclear. To address this, we conduct single-observation experiments to examine the effects of localization based on how the observation innovation is spread in space. A single observation point was placed at coordinates (x = 528 km, y = 750 km), with an observation value of 15 flashes per minute per pixel. The ensembles used in these experiments were generated from spinup forecasts initialized from the 1800 UTC GDAS analyses, as described in Fig. 2. Additionally, the percentage of retained P_b in LGETKF affects localization accuracy. A higher percentage of retained P_b can improve localization accuracy but at an increased computational cost. In the single-observation experiments, we also assess the magnitude and spatial distribution of analysis increments for LGETKF with varying percentages of retained P_b. The results are compared with PEn3DVar, which also employs model-space localization but does not rely on modulated ensembles or singular value decomposition (SVD) for its localization.

Four sets of vertical localization radii, ranging from $R_L = \ln(p/p_0) = 0.2$, 0.4, 1, and 4 (with four effectively covering the entire depth of the model domain, therefore representing effectively no vertical localization), were used for different algorithms. As shown in Fig. 5, when R_L is small (0.2 and 0.4), the analysis increments of hydrometeor mixing ratios produced by LETKF have a much smaller vertical extent (Figs. 5a,b) compared to those by LGETKF and PEn3DVar (e.g., Figs. 5m,n,q,r). This is because the R-based localization of LETKF restricts analysis increments to within the specified distance from the assumed observation height of 6.5 km, which is chosen following Allen et al. (2016) and Kong et al. (2020) to represent the mixed-phase region where lightning activity most frequently initiates. In contrast, LGETKF and PEn3DVar do not assume a specific observation height level, so that analysis increments are found at and near levels where graupel is present. A small localization radius prevents the spread of analysis increments to lower levels, where other hydrometeors, such as

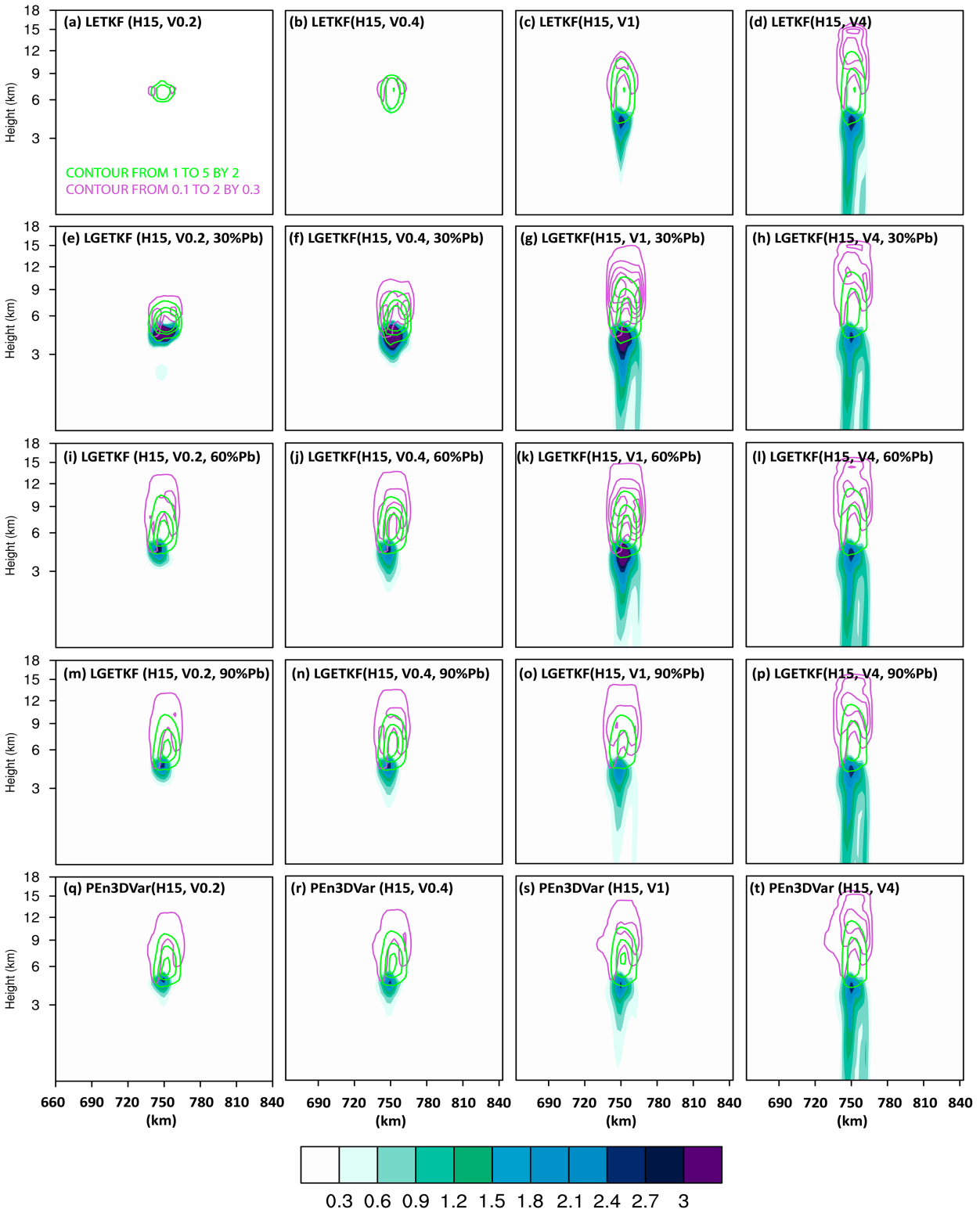

FIG. 5. Vertical cross sections of mixing ratio increments (g kg^{-1}) of rain (shading), snow (purple contours, starting from 0.1 with 0.3 g kg^{-1} intervals), and graupel (green contours, starting from 1 with 2 g kg^{-1} intervals) after the first DA with the same horizontal localization of 18 km and different vertical localizations of (a),(e),(i),(m),(q) 0.2; (b),(f),(j),(n),(r) 0.4; (c),(g),(k),(o),(s) 1; and (d),(h),(l),(p),(t) 4 in ln(p) space, using (a)–(d) LETKF, (e)–(h) LGETKF with 30% retained covariance, (i)–(l) LGETKF with 60% retained covariance, (m)–(p) LGETKF with 90% retained covariance, and (q)–(t) PEn3DVar algorithms, respectively. The cross section passes through the single observation point (x = 528 km, y = 750 km).

rainwater, might dominate. This suppression is more pronounced in LETKF compared to LGETKF and PEn3DVar, which is undesirable for observation operators involving vertical integration, such as lightning and satellite radiance data.

From a physical perspective, the FED observation operator involves a vertical integral of graupel mass; the impact of the observation is expected to extend throughout the convective column. Therefore, a vertical localization strategy that enables broader vertical spreading (i.e., with larger effective localization radii) is physically more consistent with this application.

However, larger localization radii are not always better. The purpose of covariance localization is to suppress spurious correlations that arise from limited ensemble size. Excessively large vertical radii may admit unrealistic correlations between distant levels, potentially degrading the analysis. Thus, a balance between enabling physical vertical coupling and maintaining statistical robustness is desired. To investigate this balance empirically, we perform sensitivity experiments using a range of vertical localization radii (R_L = 0.2, 0.4, 1, 4). While small R_L values are not necessarily suitable for FED observations, they serve a diagnostic purpose by revealing the behavioral differences between observation-space (LETKF) and model-space (LGETKF, En3DVar) localization. These differences are most evident in single-observation experiments that help validate algorithmic behaviors.

Three different percentages of retained P_b are tested in LGETKF and compared with PEn3DVar. Notably, retaining 90% of P_b in LGETKF results in analysis increments similar to those of PEn3DVar (as shown in the bottom two rows of Fig. 5), which agrees with expectation since both methods employ model-space vertical localization, and LGETKF has nearly complete P_b retention. When only 30% of P_b is retained, the LGETKF analysis increments of graupel mixing ratio, with a small vertical localization radius (Fig. 5e), are more vertically confined but exhibit higher magnitude compared to PEn3DVar (Fig. 5q). In contrast, retaining 60% of P_b in LGETKF produces increments that are comparable to those of PEn3DVar, even for small localization radii, suggesting that retaining 60% of P_b may be enough for achieving the desired accuracy at a relatively lower cost.

d. *Sensitivity to vertical localization scales across LETKF, LGETKF, and En3DVar*

In the previous section, single-observation experiments are conducted to gain some insights into the behaviors of the algorithms assimilating FED observations with various localization radii and retained covariance levels. In this section, we assimilate all FED observations to determine the optimal vertical localization radius and the most appropriate percentage of retained P_b. In our prior FED DA studies, we typically use a large vertical localization radius that has effectively no localization effect to allow the FED observations to influence the entire model depth (Kong et al. 2020, 2022, 2024). Here, the sensitivity experiments test the validity of such a choice.

The same set of sensitivity tests in the last subsection is run, assimilating a full set of FED data instead of a single observation. Optimal parameters are identified based on the FSS of 6-h reflectivity forecasts following 1-h FED data assimilation with 5-min cycles, following the procedures outlined in Fig. 2. Intentionally, this study does not explore variations in the horizontal localization radius. Taking into account the FED observation pixel resolution of ~10 km, an 18-km horizontal localization radius is selected following the guidance of previous studies (Mansell 2014; Kong et al. 2020, 2022, 2024). This radius is larger than both the observation pixel size and the 3-km grid spacing of the model, ensuring that each grid point is influenced by at least two FED observations to avoid too noisy analysis increments. It also avoids noise that can be introduced by distant covariances. The 18-km horizontal localization radius corresponds to the cutoff distance at which the Gaspari–Cohn localization function becomes zero in LETKF and LGETKF. The same horizontal localization length scale is applied in En3DVar via the BUMP-generated localization matrix.

The LETKF algorithm using vertical localization radii R_L = 0.2, 0.4, 1, and 4 shows subtle yet noticeable variations in FSS performance for composite reflectivity at a 20-dBZ threshold (Fig. 6a). Because capturing convective structures is more challenging at high thresholds, we focus here on lower thresholds for the overall convective system structure. According to Fig. 6a, the LETKF_V4 variant, with R_L = 4, generally shows higher forecast accuracy across these metrics. Similarly, other LGETKF variants, particularly for R_L = 4, perform marginally better (Fig. 6b). Among the LGETKF variants, retaining a covariance of 60% strikes an optimal balance between performance and computational efficiency (section 4c), as in the case of single observation tests. In contrast, the PEn3DVar algorithm, particularly for R_L = 4, displays more pronounced differences and achieves higher FSS than its counterparts (Figs. 6c,d).

While these sensitivity tests with LETKF, LGETKF, and PEn3DVar show some differences, the differences are not significant. The V4 variants of both LETKF and LGETKF, particularly with 60% retained covariance in LGETKF, show marginally better FSS performance for composite reflectivity. In addition to this slight performance advantage, the R_L = 4 configuration is also the most computationally efficient, as it avoids excessive localization computations in the vertical. Considering both forecast performance and runtime efficiency, the largest vertical localization radius (R_L = 4) and 60% retained P_b are chosen as the optimal settings for our experiments. This study therefore validates the earlier use of a large vertical localization radius for FED assimilation.

5. Overall performance evaluation of LDA with LETKF, LGETKF, and PEn3DVar

In the previous section, optimal vertical localization radius R_L = 4 for all DA methods and a 60% retained P_b for LGETKF are determined. This section performs further evaluations on the performance of LETKF, LGETKF, and PEn3DVar algorithms with these settings, through both statistical verification and subjective evaluation of lightning and reflectivity forecasts.

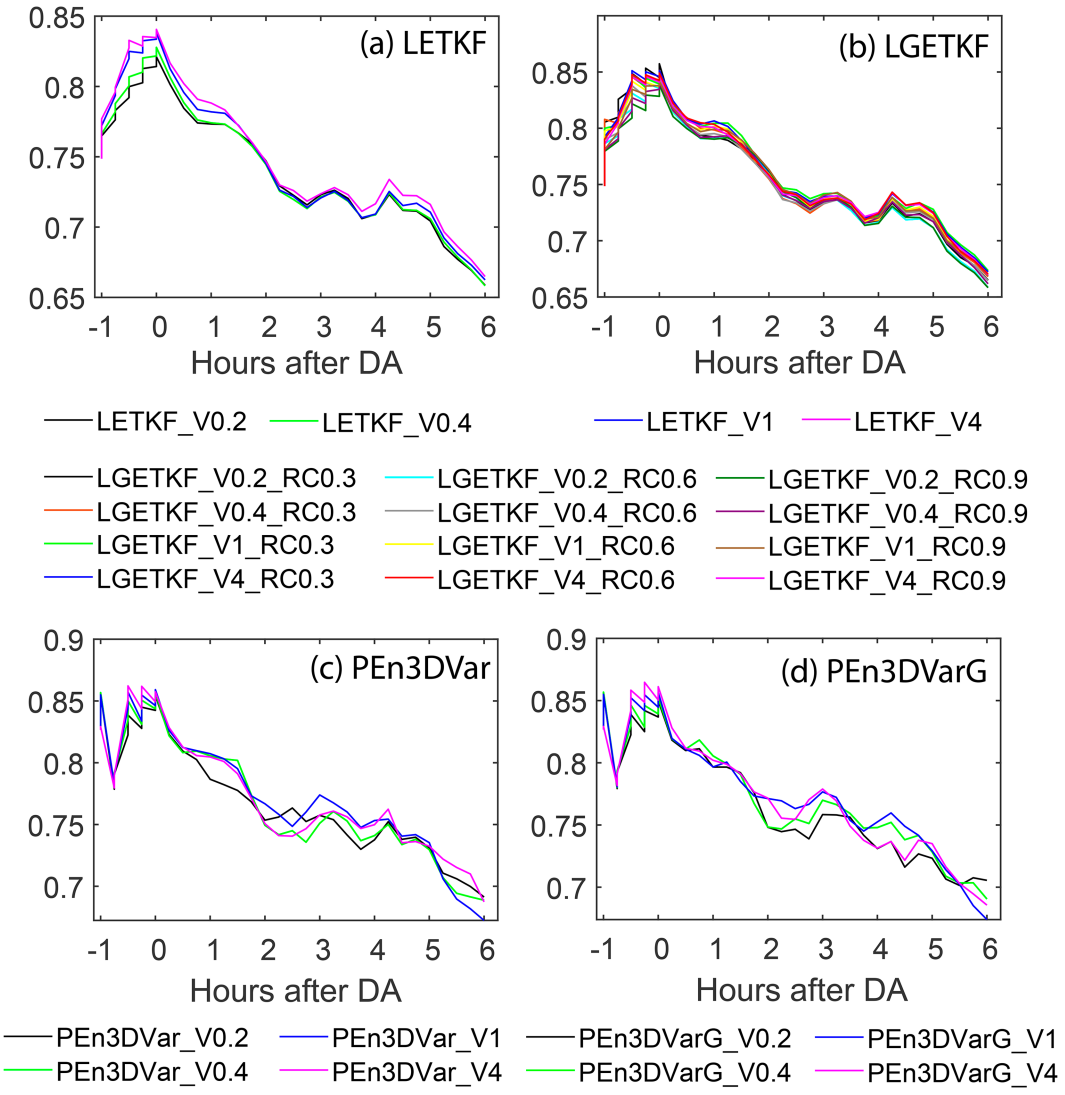

FIG. 6. FSS for composite reflectivity at the 20-dBZ threshold, evaluated within a 1-h DA window and forecast periods from 0 to 6 h. (a),(b) Results from DA experiments using LETKF and LGETKF algorithms with varying vertical localization radii R_L = 0.2, 0.4, 1, and 4 (indicated by _V followed by the R_L number). LGETKF variants with different retained covariance (indicated by _RC followed by a fraction number) percentages are also shown. (c),(d) Results from PEn3DVar experiments (PEn3DVar and PEn3DVarG), which are coupled with LETKF and LGETKF and use the same localization radii. Only the mean FSS results for both LETKF and LGETKF are presented for clarity.

The FSSs for the analyses and forecasts verified against observed FED and composite reflectivity are shown in Fig. 7 for LETKF, LGETKF, PEn3DVar, and PEn3DVarG as well as NoDA experiments. Figures 7a and 7b show the FSS for FED at thresholds of 1 and 5 flashes per minute per pixel, respectively, while Figs. 7c and 7d depict the FSS for composite reflectivity at thresholds of 20 and 35 dBZ. The results are shown within the 1-h DA window and across the 0–6-h free forecast periods.

The figure demonstrates that LDA experiments generally yield higher FSS values than NoDA. Specifically, LETKF and LGETKF show superior performance for FED thresholds in the initial forecast hours after DA (Figs. 7a,b). Likewise, PEn3DVar and PEn3DVarG demonstrate improved FSS, particularly for the 20-dBZ reflectivity threshold during the free-forecast periods (Figs. 7c,d). These results highlight the positive impacts of assimilating FED data in improving the accuracy of forecasts in terms of both FED and composite reflectivity, even though no reflectivity data are assimilated.

While NoDA shows slightly higher FSS values at the 35-dBZ threshold during certain forecast hours (Fig. 7d), this appears to be partially due to overprediction in the northern portion of the storm system, which increases spatial overlap with observed high reflectivity regions. In contrast, DA experiments more successfully capture the southern convective core that is largely missed in NoDA, but the slight spatial displacements in the forecasts of DA experiments limit improvement

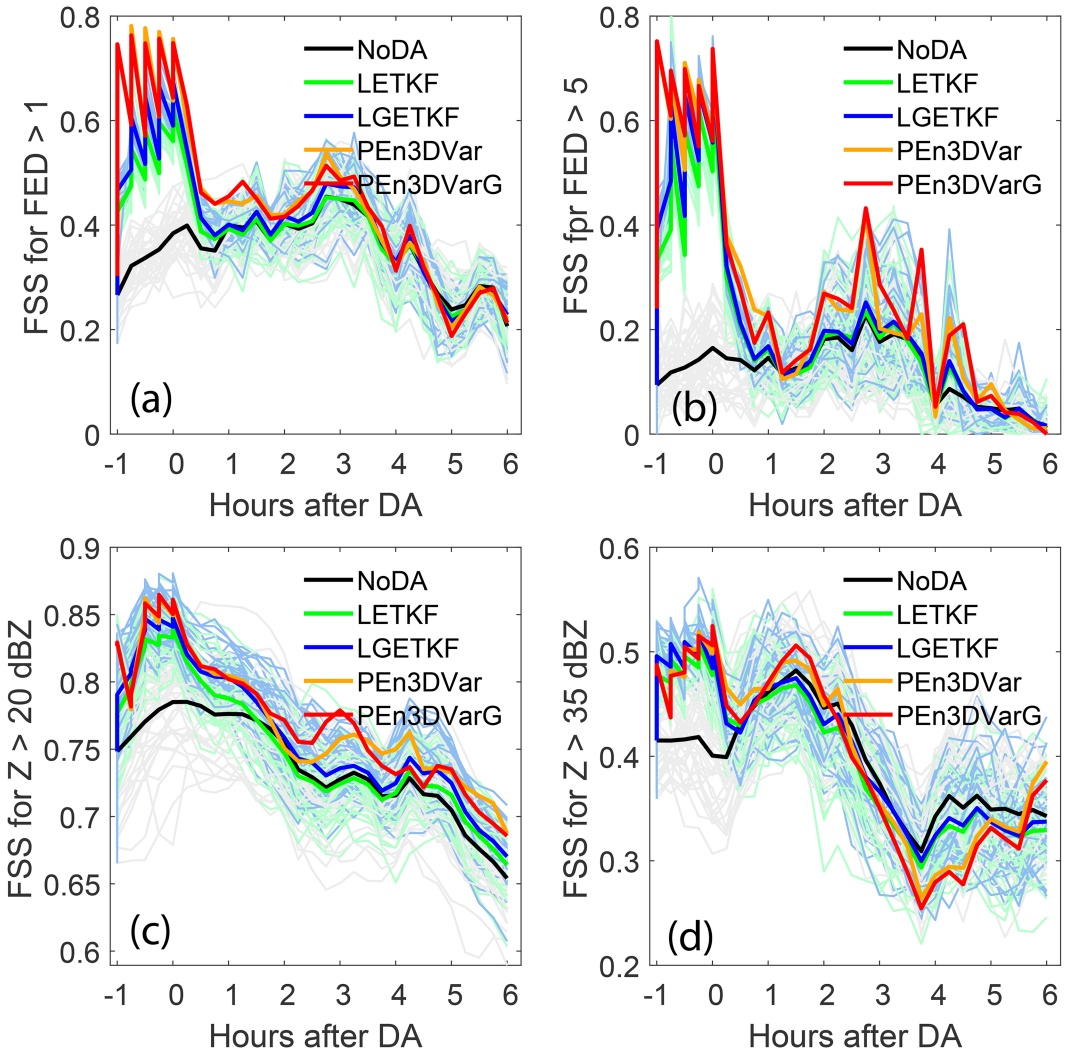

FIG. 7. FSS for (top) analyses and forecasts of FED at thresholds of 1 and 5 flashes per minute per pixel and (bottom) composite reflectivity at thresholds of 20 and 35 dBZ. The results are presented within the 1-h DA window and across the 0–6-h free-forecast periods. The figure includes comparisons between NoDA and DA experiments using LETKF, LGETKF, PEn3DVar, and PEn3DVarG. Bold lines represent the ensemble mean for NoDA, LETKF, and LGETKF (average of 40 members), while thin lines of the same color represent individual ensemble members. Deterministic results of PEn3DVar and PEn3DVarG are depicted by a single bold line.

in FSS. This suggests that FSS alone may not fully reflect improvements in storm structure and intensity captured by the DA methods. These effects are discussed further in the next section based on subjective verification of reflectivity forecasts.

Performance diagrams, as introduced by Roebber (2009), can provide a more comprehensive assessment of the skills of forecasts. Figure 8 shows that all DA experiments outperform NoDA in forecasting both FED and composite reflectivity, especially in terms of FED in earlier forecasts. This superiority is evidenced in two key metrics: a higher critical success index (CSI), indicated by the shaded contours (the closer to the top-right corner, the higher is the CSI score), and a lower bias, indicated by the dashed lines (no bias along the lower-left to top-right corner line of 1). During the first hour of the forecast, the improvement in the forecast accuracy and reliability of the DA experiments over NoDA is more evident. While this difference diminishes over time, it remains notable up to 2 h postassimilation, underscoring the sustained impact of the lightning DA. For CSI, PEn3DVar and PEn3DVarG have overall slightly higher scores than LETKF and LGETKF (Fig. 8). It is also true for biases for most of the forecasts between 1 and 2 h. The DA experiments also have slightly lower biases (close to 1) than NoDA experiments, especially in the latter half of the 2-h forecast window.

Since FED is directly assimilated in our study, we focus on comparing the forecasts of this parameter in our subjective evaluation in Fig. 9. The figure compares 1–4-h FED forecasts from various DA experiments with NoDA and with matching observations. The DA experiments, particularly PEn3DVar

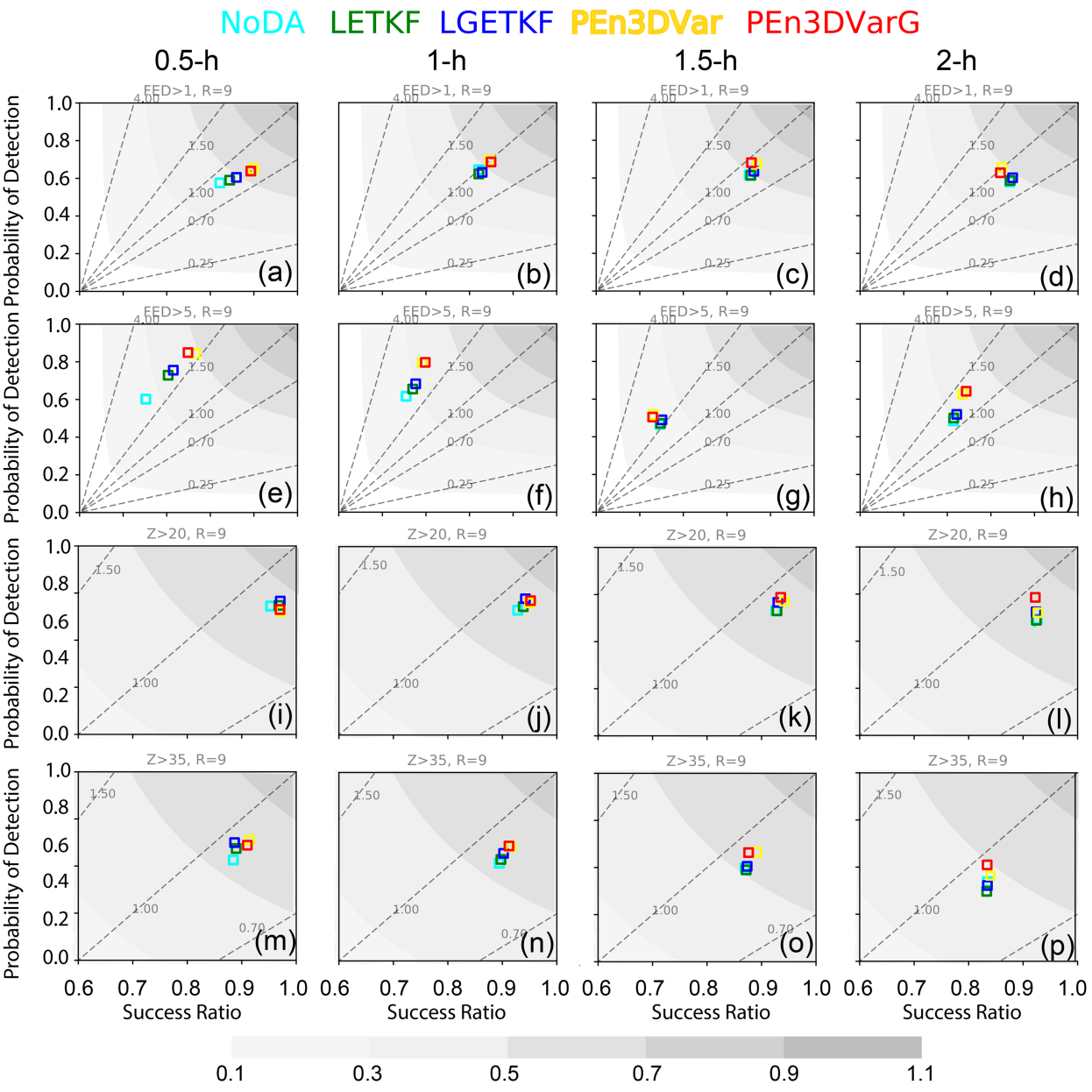

FIG. 8. Performance diagrams for FED and composite reflectivity forecasts across various thresholds and time frames, using a 9-km neighborhood radius. (a)–(d) The 0.5–2-h FED forecasts after DA with a threshold of 1 flash per minute per pixel. (e)–(h) The same time intervals for FED forecasts with a threshold of 5 flashes per minute per pixel. (i)–(l) The 0.5–2-h composite reflectivity forecasts at a 20-dBZ threshold and (m)–(p) forecasts at a 35-dBZ threshold. Forecast systems include NoDA (cyan), LETKF (green), LGETKF (blue), PEn3DVar (magenta), and PEn3DVarG (red). Ensemble means for LETKF, LGETKF, and NoDA are represented by colored boxes, while En3DVar, being a single member system, is directly represented by a box.

and PEn3DVarG, show notable improvements over NoDA, especially in capturing convective activities in the southwestern parts of the convective system, where lightning activity is more prevalent. PEn3DVar and PEn3DVarG demonstrate similar effectiveness and slightly outperform LETKF and LGETKF. These results further indicate the benefits of assimilating lightning data in predicting, e.g., lightning patterns that are better aligned with observations up to 3–4 h.

In addition to analyzing FED forecasts, we further assess the ensemble neighborhood probabilities for 1–4-h composite reflectivity forecasts. Figure 10 shows the probability of reflectivity forecasts exceeding the 20-dBZ threshold, while Fig. 11 shows those for the 35-dBZ threshold. The observed composite reflectivity contours of the corresponding threshold are overlaid in black in the figures for different experiments. Consistent with the FED forecasts, PEn3DVar and

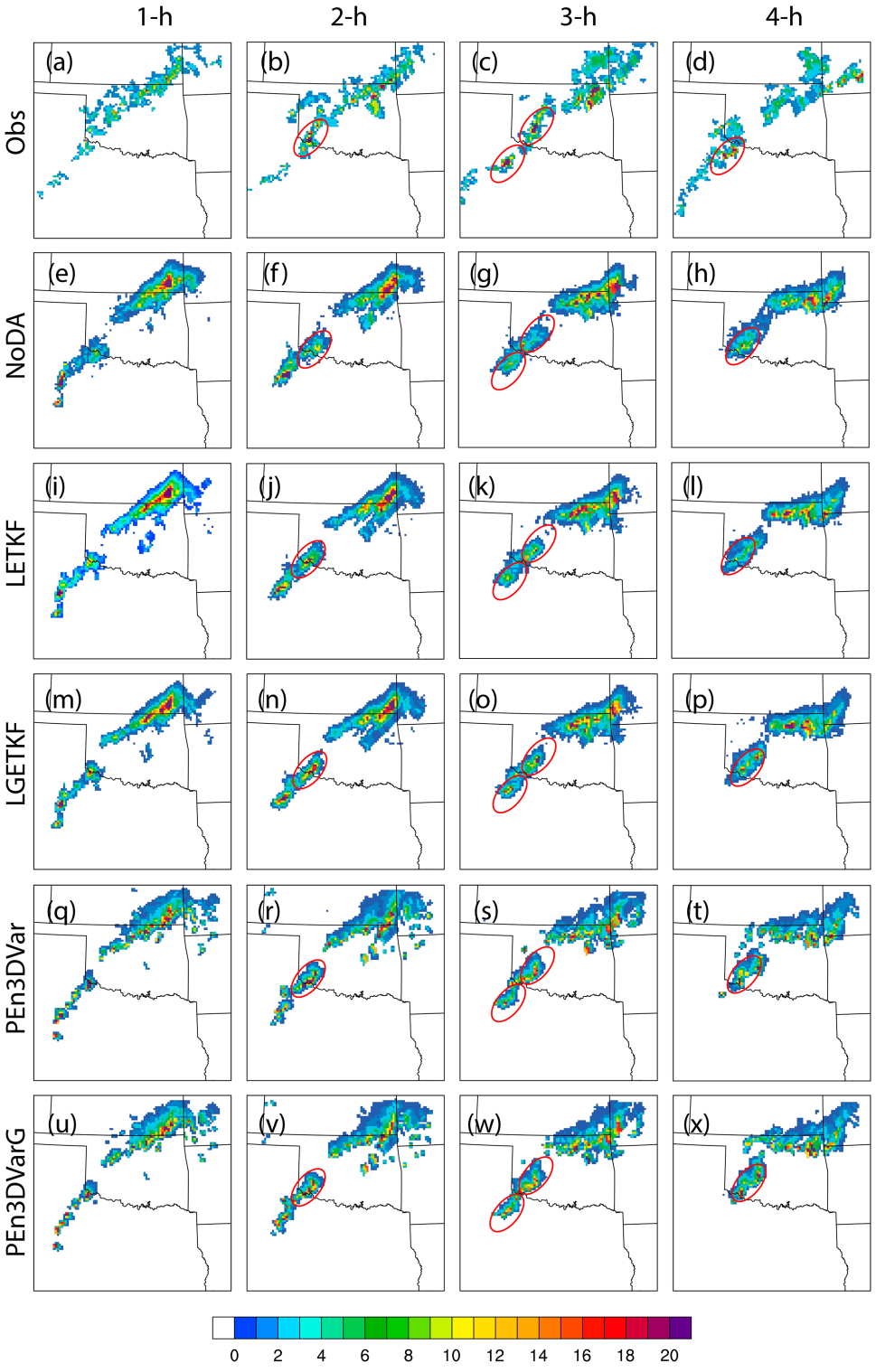

FIG. 9. Observed and forecasted FED over 1–4 hours: (a)–(d) observations, while forecasts are presented for (e)–(h) NoDA, (i)–(l) LETKF, (m)–(p) LGETKF, (q)–(t) PEn3DVar, and (u)–(x) PEn3DVarG. Shown are (a),(e),(i),(m),(q), 1-; (b),(f),(j),(n),(r) 2-; (c),(g),(k),(o),(s) 3-; and (d),(h),(l),(p),(t) 4-h forecasts.

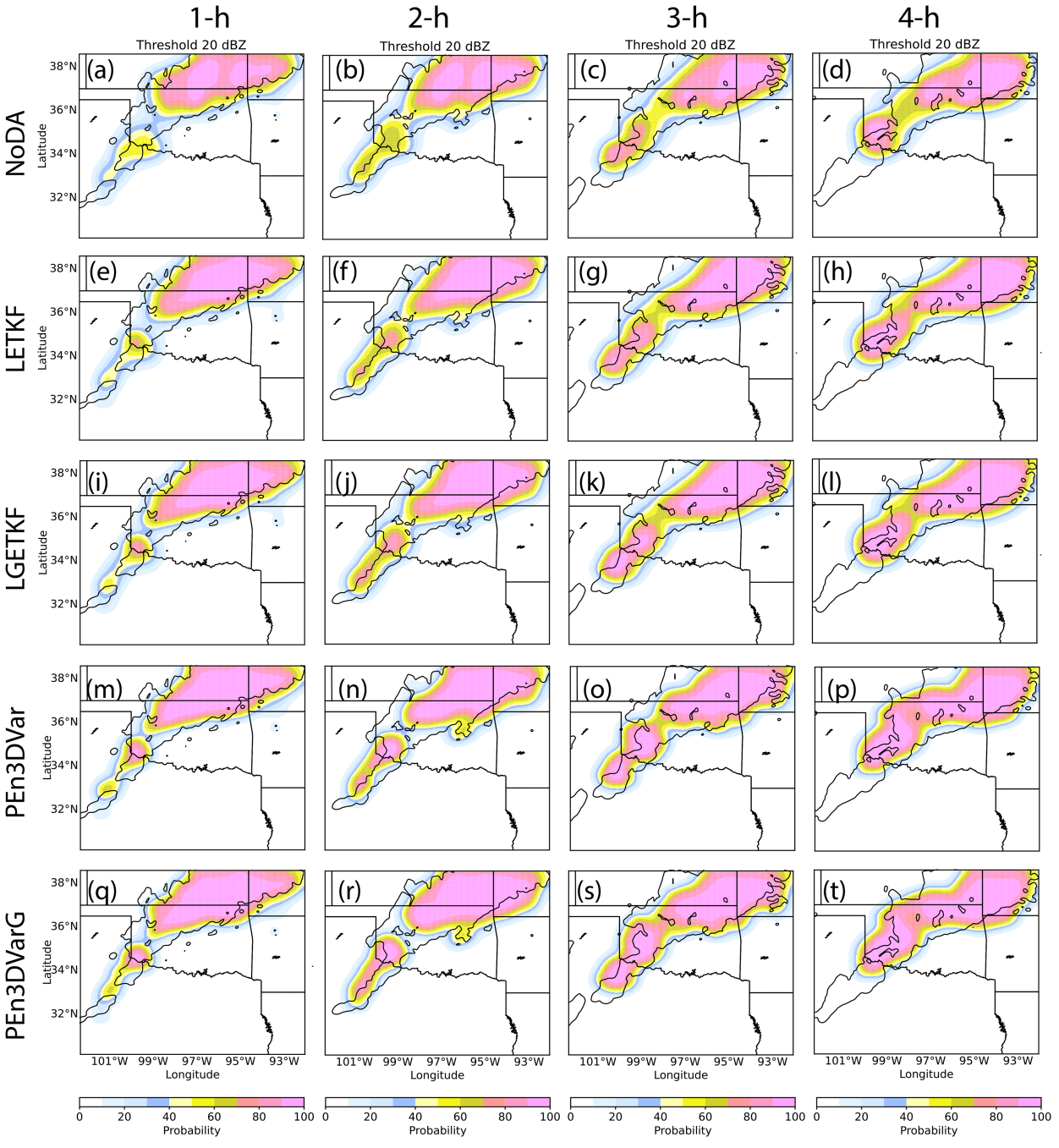

FIG. 10. Ensemble neighborhood probabilities for 1–4-h composite reflectivity forecasts exceeding 20 dB*Z* from (a)–(d) NoDA, (e)–(h) LETKF, (i)–(l) LGETKF, (m)–(p) PEn3DVar, and (q)–(t) PEn3DVarG, overlaid with MRMS composite reflectivity observations for the same threshold (black contour).

PEn3DVarG show slightly better forecast accuracy compared to LETKF and LGETKF. All DA methods show significant improvement over NoDA, particularly in the southwest regions of the convective system, where NoDA tends to underestimate reflectivity. The results further highlight the value of lightning DA in improving short-term forecasts of convective storms.

We examine further hourly accumulated precipitation forecasts. Evaluation of precipitation provides more insight on the hydrological aspects of the forecast. The probability-matched ensemble mean hourly accumulated precipitation forecasts from LETKF, LGETKF, and NoDA, and the deterministic hourly accumulated precipitation forecasts of experiments PEn3DVar and PEn3DVarG are shown in Fig. 12, with

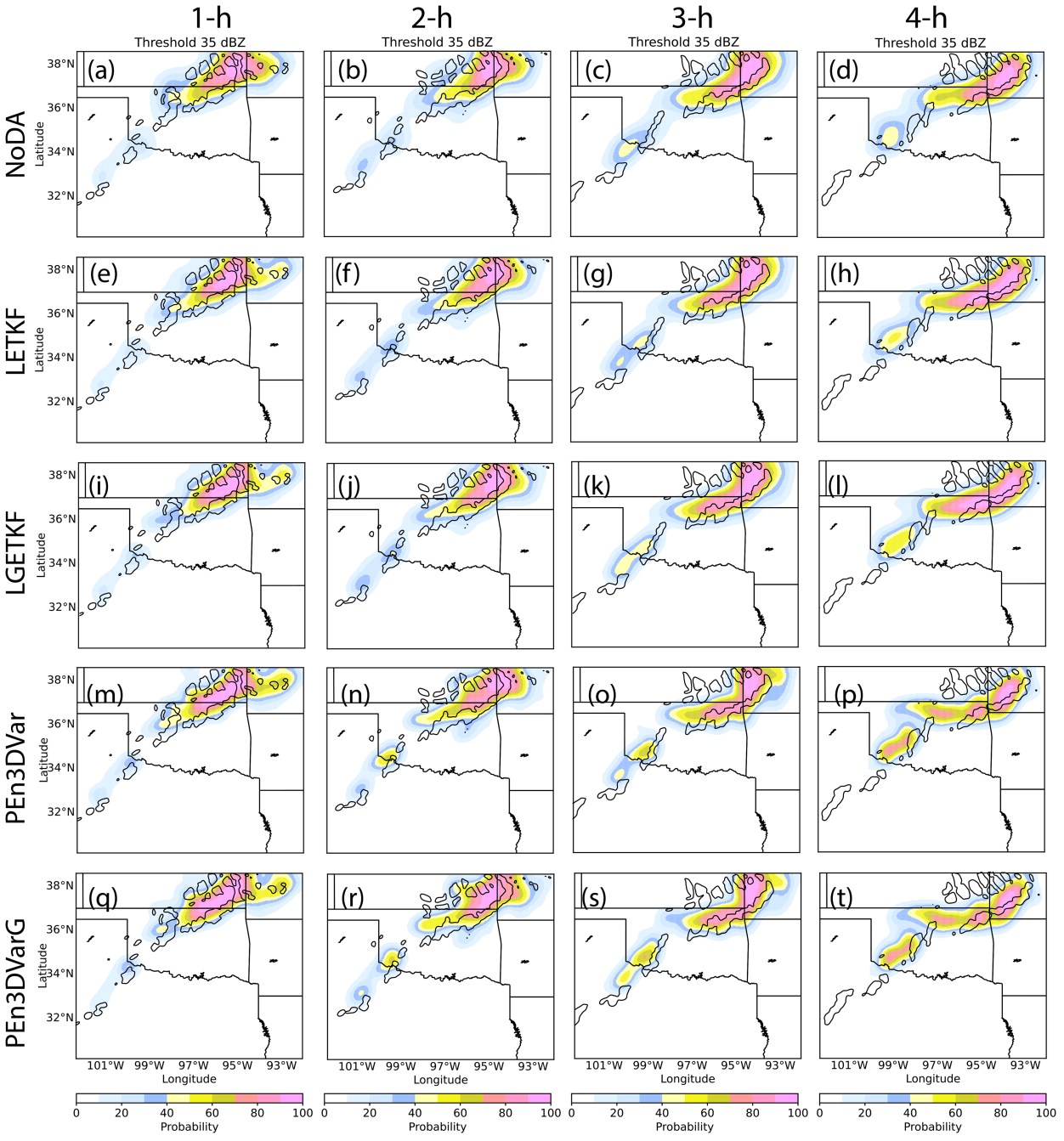

FIG. 11. Ensemble neighborhood probabilities for 1–4-h composite reflectivity forecasts exceeding 35 dB*Z* from (a)–(d) NoDA, (e)–(h) LETKF, (i)–(l) LGETKF, (m)–(p) PEn3DVar, and (q)–(t) PEn3DVarG (%), overlaid with MRMS composite reflectivity observations for the same threshold (black contour).

estimated precipitation observations by the Multi-Radar Multi-Sensor (MRMS; Zhang et al. 2016b) system overlaid, for forecast hours 1 through 4.

The figures show that all DA methods improve precipitation forecasts, particularly in capturing storm patterns missed by NoDA. While LETKF and LGETKF outperform NoDA in tracking the southwestern storms, they are less effective than PEn3DVar and PEn3DVarG. This difference becomes more pronounced in longer-range forecasts (3–4 h), where the LETKF and LGETKF tend to underpredict precipitation intensity. In contrast, PEn3DVar and PEn3DVarG consistently provide accurate predictions of intense precipitation in the southwest, aligning more closely with MRMS observations.

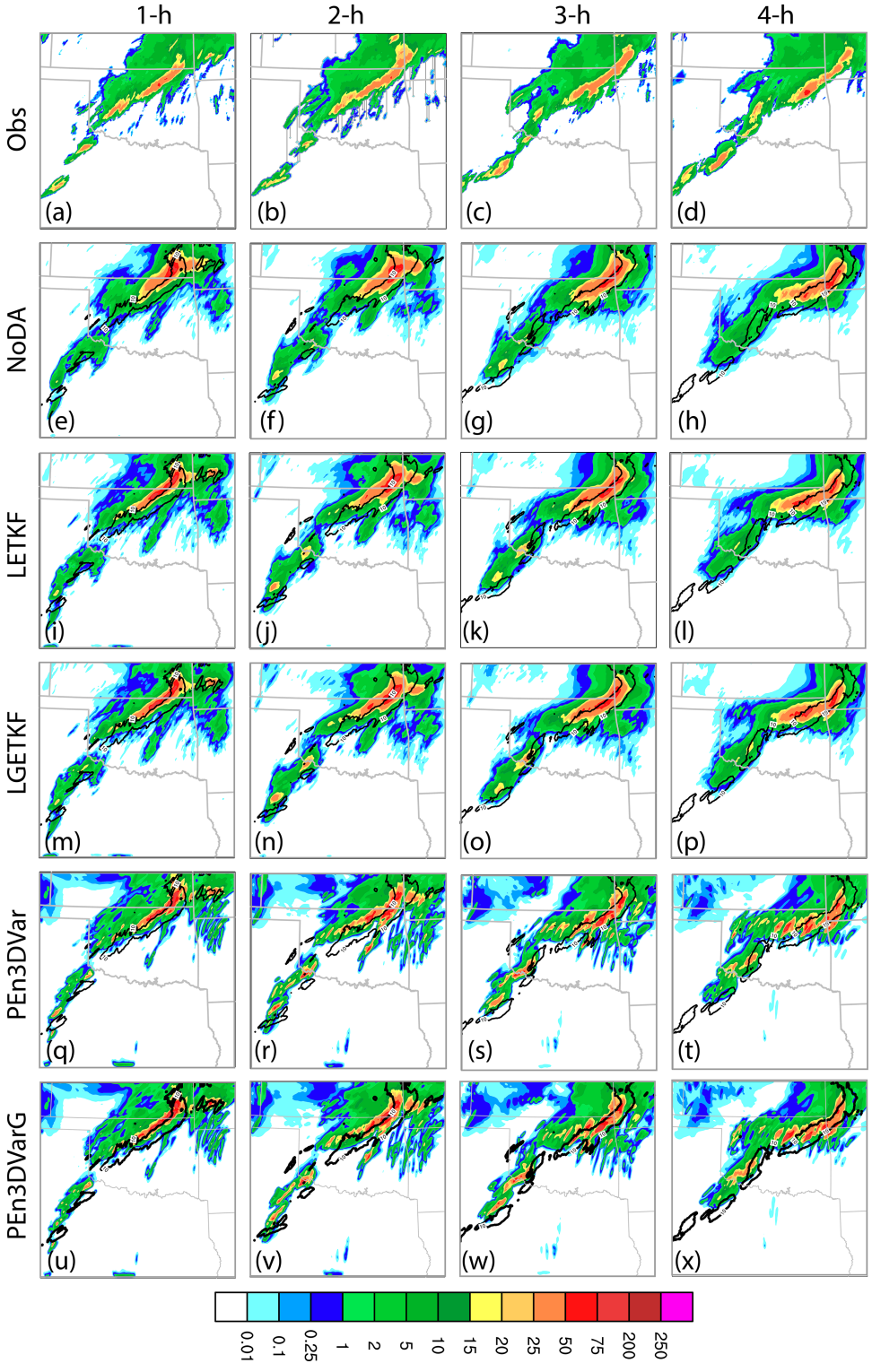

FIG. 12. Probability-matched mean hourly accumulated precipitation forecasts from NoDA, LETKF, and LGETKF, deterministic forecasts of PEn3DVar and PEn3DVarG, overlaid with MRMS-estimated hourly precipitation in black contours.

6. Summary and conclusions

In this study, we implemented the capabilities to assimilate GOES-R GLM flash extent density data within the JEDI system, integrated with the FV3-LAM dynamical core that is intended to be used by RRFSv1. The JEDI DA system is also intended to be used by RRFSv2 and other future operational forecasting systems of the NWS. The primary goal is to validate the implementation and evaluate the performance of various data assimilation methods, the LETKF, LGETKF, and En3DVar algorithms within the JEDI framework, including comparisons of their vertical localization strategies, computational efficiency, memory usage, and resulting forecast accuracy for a test case. Convergence behavior of En3DVar is consistent with expectations.

Our computational cost analysis showed that LGETKF requires significantly more resources when relatively small vertical localization radii are used or when higher percentages of retained covariance are desired, leading to higher computational costs compared to LETKF and En3DVar. The cost of LETKF does not change much with the vertical localization radius. PEn3DVar has a slightly better performance in terms of forecast accuracy at a reasonable computational cost, although the current implementation requires an order of magnitude more memory than both LETKF and LGETKF. It should be noted that PEn3DVar does require the running of either LETKF or LGETKF, which provides the ensemble perturbations for flow-dependent covariance. Therefore, running the En3DVar requires an additional computational step.

To better understand the behaviors of the three algorithms, in particular in terms of the effects of different vertical localization treatments in these algorithms, for the assimilation of lightning FED data whose observation operator involves vertical integration through the model column depth, single FED observation experiments were run. Vertical localization radii R_L equaling to 0.2, 0.4, 1, and 4 in the $\ln(p/p_0)$ space were examined. Significant differences exist among the algorithms when the radius is small compared to the model domain depth because the localization is in observation space for LETKF and model space for LGETKF and En3DVar. When large R_L is used so that there is effectively no vertical localization, the three algorithms perform very similarly. Given the nature of the FED observation operator, and based on sensitivity experiments, large values of $R_L = 4$ are found to be preferred, and subsequent experiments and evaluations for a test case use this value. Furthermore, retaining 60% of the background error covariance when performing vertical localization in the gain-form LETKF is found to be sufficiently accurate, saving some computational costs.

Fraction skill scores for FED and composite reflectivity forecasts are calculated against observations up to 6 h, and performance diagrams are plotted for the forecasts up to 2 h. Subjective evaluations of the forecasts are performed for forecast FED, neighborhood ensemble probabilities of composite reflectivity for two thresholds, and hourly accumulated precipitation forecasts up to 4 h. These evaluations show that the FED DA experiments generally clearly outperform the experiment where FED data are not assimilated, and among the DA experiments, the En3DVar algorithm coupled with LETKF or LGETKF slightly outperforms the two forms of LETKF algorithms. Comparing the algorithms in general and determining which one is better is not the main goal of this paper—the main goal is to validate our implementation of FED DA within various algorithms in JEDI, and such capabilities may potentially be used in future operational NWP systems of the NWS, including the RRFS.

A noted limitation of this study is the use of a single test case. This can limit the generalizability of the findings in terms of the DA impact and relative performance of the algorithms. While the current design focuses on a single 1-h FED DA cycling period followed by a 6-h forecast, future research should expand the evaluations across multiple weather scenarios and cases to further assess the effectiveness and robustness of the LDA capabilities.

Acknowledgments. This research was primarily supported by NOAA JTTI Grant (NA21OAR4590165) and the NOAA R2O Program support through the NOAA–University of Oklahoma Cooperative Agreement (NA21OAR4320204). Computational resources were furnished by the NSF supercomputing facility at the Texas Advanced Computing Center with allocations acquired through the ACCESS program.

Data availability statement. The GLM level-II lightning detection data used in this study are publicly available from the NOAA National Centers for Environmental Information (NCEI) at https://www.ncdc.noaa.gov/airs-web/search (under the product selection menu, choose "GLM L2 + Lightning Detection Data.") The raw data are postprocessed to derive flash extent density (FED) using established procedures [e.g., spatial gridding and temporal aggregation following Bruning et al. (2019)] and subsequently converted into the HDF5-based observation format required by the JEDI data assimilation system. To support reproducibility, a subset of the data used in this study—including processed GLM FED observations, FV3 model background fields, and configuration files—is permanently archived at the Harvard Dataverse: (https://doi.org/10.7910/DVN/B4NZZM).

REFERENCES

Aksoy, A., D. C. Dowell, and C. Snyder, 2009: A multicase comparative assessment of the ensemble Kalman filter for assimilation of radar observations. Part I: Storm-scale analyses. *Mon. Wea. Rev.*, **137**, 1805–1824, https://doi.org/10.1175/2008MWR2691.1.

——, ——, and ——, 2010: A multicase comparative assessment of the ensemble Kalman filter for assimilation of radar observations. Part II: Short-range ensemble forecasts. *Mon. Wea. Rev.*, **138**, 1273–1292, https://doi.org/10.1175/2009MWR3086.1.

Alexander, G. D., J. A. Weinman, V. M. Karyampudi, W. S. Olson, and A. C. L. Lee, 1999: The effect of assimilating rain rates derived from satellites and lightning on forecasts of the 1993 Superstorm. *Mon. Wea. Rev.*, **127**, 1433–1457, https://doi.org/10.1175/1520-0493(1999)127<1433:TEOARR>2.0.CO;2.

Allen, B. J., E. R. Mansell, D. C. Dowell, and W. Deierling, 2016: Assimilation of pseudo-GLM data using the ensemble Kalman filter. *Mon. Wea. Rev.*, **144**, 3465–3486, https://doi.org/10.1175/MWR-D-16-0117.1.

Banos, I. H., W. D. Mayfield, G. Ge, L. F. Sapucci, J. R. Carley, and L. Nance, 2022: Assessment of the data assimilation framework for the Rapid Refresh Forecast System v0.1 and impacts on forecasts of a convective storm case study. *Geosci. Model Dev.*, **15**, 6891–6917, https://doi.org/10.5194/gmd-15-6891-2022.

Bauer, P., A. Thorpe, and G. Brunet, 2015: The quiet revolution of numerical weather prediction. *Nature*, **525**, 47–55, https://doi.org/10.1038/nature14956.

Bishop, C. H., B. J. Etherton, and S. J. Majumdar, 2001: Adaptive sampling with the ensemble transform Kalman filter. Part I: Theoretical aspects. *Mon. Wea. Rev.*, **129**, 420–436, https://doi.org/10.1175/1520-0493(2001)129<0420:ASWTET>2.0.CO;2.

——, J. S. Whitaker, and L. Lei, 2017: Gain form of the ensemble transform Kalman filter and its relevance to satellite data assimilation with model space ensemble covariance localization. *Mon. Wea. Rev.*, **145**, 4575–4592, https://doi.org/10.1175/MWR-D-17-0102.1.

Bruning, E. C., and Coauthors, 2019: Meteorological imagery for the Geostationary Lightning Mapper. *J. Geophys. Res. Atmos.*, **124**, 14 285–14 309, https://doi.org/10.1029/2019JD030874.

Chang, D. E., J. A. Weinman, C. A. Morales, and W. S. Olson, 2001: The effect of spaceborne microwave and ground-based continuous lightning measurements on forecasts of the 1998 Groundhog Day storm. *Mon. Wea. Rev.*, **129**, 1809–1833, https://doi.org/10.1175/1520-0493(2001)129<1809:TEOSMA>2.0.CO;2.

Courtier, P., J.-N. Thepaut, and A. Hollingsworth, 1994: A strategy for operational implementation of 4D-Var, using an incremental approach. *Quart. J. Roy. Meteor. Soc.*, **120**, 1367–1387, https://doi.org/10.1002/qj.49712051912.

Derber, J. C., D. F. Parrish, and S. J. Lord, 1991: The new global operational analysis system at the National Meteorological Center. *Wea. Forecasting*, **6**, 538–547, https://doi.org/10.1175/1520-0434(1991)006<0538:TNGOAS>2.0.CO;2.

Dowell, D. C., and Coauthors, 2022: The High-Resolution Rapid Refresh (HRRR): An hourly updating convection-allowing forecast model. Part I: Motivation and system description. *Wea. Forecasting*, **37**, 1371–1395, https://doi.org/10.1175/WAF-D-21-0151.1.

Ek, M. B., K. E. Mitchell, Y. Lin, E. Rogers, P. Grunmann, V. Koren, G. Gayno, and J. D. Tarpley, 2003: Implementation of the upgraded Noah land-surface model in the National Centers for Environmental Prediction operational mesoscale Eta model. *J. Geophys. Res.*, **108**, 8851, https://doi.org/10.1029/2002JD003296.

Evensen, G., 1994: Sequential data assimilation with a nonlinear quasi-geostrophic model using Monte Carlo methods to forecast error statistics. *J. Geophys. Res.*, **99**, 10143–10162, https://doi.org/10.1029/94JC00572.

Fierro, A. O., E. R. Mansell, C. L. Ziegler, and D. R. MacGorman, 2012: Application of a lightning data assimilation technique in the WRF-ARW Model at cloud-resolving scales for the tornado outbreak of 24 May 2011. *Mon. Wea. Rev.*, **140**, 2609–2627, https://doi.org/10.1175/MWR-D-11-00299.1.

——, J. Gao, C. L. Ziegler, E. R. Mansell, D. R. MacGorman, and S. R. Dembek, 2014: Evaluation of a cloud-scale lightning data assimilation technique and a 3DVAR method for the analysis and short-term forecast of the 29 June 2012 derecho event. *Mon. Wea. Rev.*, **142**, 183–202, https://doi.org/10.1175/MWR-D-13-00142.1.

——, E. R. Mansell, C. L. Ziegler, and D. R. MacGorman, 2015: Explicitly simulated electrification and lightning within a tropical cyclone based on the environment of Hurricane Isaac (2012). *J. Atmos. Sci.*, **72**, 4167–4193, https://doi.org/10.1175/JAS-D-14-0374.1.

——, J. Gao, C. L. Ziegler, K. M. Calhoun, E. R. Mansell, and D. R. MacGorman, 2016: Assimilation of flash extent data in the variational framework at convection-allowing scales: Proof-of-concept and evaluation for the short-term forecast of the 24 May 2011 tornado outbreak. *Mon. Wea. Rev.*, **144**, 4373–4393, https://doi.org/10.1175/MWR-D-16-0053.1.

——, Y. Wang, J. Gao, and E. R. Mansell, 2019: Variational assimilation of radar data and GLM lightning-derived water vapor for the short-term forecasts of high-impact convective events. *Mon. Wea. Rev.*, **147**, 4045–4069, https://doi.org/10.1175/MWR-D-18-0421.1.

Gao, J., and D. J. Stensrud, 2012: Assimilation of reflectivity data in a convective-scale, cycled 3DVAR framework with hydrometeor classification. *J. Atmos. Sci.*, **69**, 1054–1065, https://doi.org/10.1175/JAS-D-11-0162.1.

Ge, G., M. Hu, S. Weygandt, and C. Alexander, 2019: The impact of GOES-16 GLM lightning observations on the RAP/HRRR assimilation and forecasts. *15th Annual Symposium on New Generation Operational Environmental Satellite Systems*, Phoenix, AZ, Amer. Meteor. Soc., https://ams.confex.com/ams/2019Annual/webprogram/Paper350287.html.

Goodman, S. J., and Coauthors, 2013: The GOES-R Geostationary Lightning Mapper (GLM). *Atmos. Res.*, **125-126**, 34–49, https://doi.org/10.1016/j.atmosres.2013.01.006.

Greybush, S. J., E. Kalnay, T. Miyoshi, K. Ide, and B. R. Hunt, 2011: Balance and ensemble Kalman filter localization techniques. *Mon. Wea. Rev.*, **139**, 511–522, https://doi.org/10.1175/2010MWR3328.1.

Hamill, T. M., and C. Snyder, 2000: A hybrid ensemble Kalman filter–3D variational analysis scheme. *Mon. Wea. Rev.*, **128**, 2905–2919, https://doi.org/10.1175/1520-0493(2000)128<2905:AHEKFV>2.0.CO;2.

Harris, L., X. Chen, W. Putman, L. Zhou, and J.-H. Chen, 2021: A scientifc description of the GFDL Finite-Volume Cubed-Sphere Dynamical Core. NOAA Tech. Memo., OAR GFDL 2021-001, https://repository.library.noaa.gov/view/noaa/30725.

Heinzeller, D., L. Bernardet, G. Firl, M. Zhang, X. Sun, and M. Ek, 2023: The Common Community Physics Package (CCPP) framework v6. *Geosci. Model Dev.*, **16**, 2235–2259, https://doi.org/10.5194/gmd-16-2235-2023.

Honda, T., and Coauthors, 2018: Assimilating all-sky *Himawari-8* satellite infrared radiances: A case of Typhoon Soudelor (2015). *Mon. Wea. Rev.*, **146**, 213–229, https://doi.org/10.1175/MWR-D-16-0357.1.

Hu, J., A. O. Fierro, Y. Wang, J. Gao, and E. R. Mansell, 2020: Exploring the assimilation of GLM-derived water vapor mass in a cycled 3DVAR framework for the short-term forecasts of high-impact convective events. *Mon. Wea. Rev.*, **148**, 1005–1028, https://doi.org/10.1175/MWR-D-19-0198.1.

Hu, M., M. Xue, and K. Brewster, 2006a: 3DVAR and cloud analysis with WSR-88D level-II data for the prediction of the Fort Worth, Texas, tornadic thunderstorms. Part I: Cloud analysis and its impact. *Mon. Wea. Rev.*, **134**, 675–698, https://doi.org/10.1175/MWR3092.1.

——, ——, J. Gao, and K. Brewster, 2006b: 3DVAR and cloud analysis with WSR-88D level-II data for the prediction of the

Fort Worth, Texas, tornadic thunderstorms. Part II: Impact of radial velocity analysis via 3DVAR. *Mon. Wea. Rev.*, **134**, 699–721, https://doi.org/10.1175/MWR3093.1.

Hunt, B. R., E. J. Kostelich, and I. Szunyogh, 2007: Efficient data assimilation for spatiotemporal chaos: A local ensemble transform Kalman filter. *Physica D*, **230**, 112–126, https://doi.org/10.1016/j.physd.2006.11.008.

James, E. P., and Coauthors, 2022: The High-Resolution Rapid Refresh (HRRR): An hourly updating convection-allowing forecast model. Part II: Forecast performance. *Wea. Forecasting*, **37**, 1397–1417, https://doi.org/10.1175/WAF-D-21-0130.1.

Jones, T. A., X. Wang, P. Skinner, A. Johnson, and Y. Wang, 2018: Assimilation of *GOES-13* imager clear-sky water vapor (6.5 μm) radiances into a warn-on-forecast system. *Mon. Wea. Rev.*, **146**, 1077–1107, https://doi.org/10.1175/MWR-D-17-0280.1.

——, and Coauthors, 2020: Assimilation of *GOES-16* radiances and retrievals into the warn-on-forecast system. *Mon. Wea. Rev.*, **148**, 1829–1859, https://doi.org/10.1175/MWR-D-19-0379.1.

Jung, Y., M. Xue, G. Zhang, and J. M. Straka, 2008: Assimilation of simulated polarimetric radar data for a convective storm using the ensemble Kalman filter. Part II: Impact of polarimetric data on storm analysis. *Mon. Wea. Rev.*, **136**, 2246–2260, https://doi.org/10.1175/2007MWR2288.1.

Kain, J. S., and Coauthors, 2008: Some practical considerations regarding horizontal resolution in the first generation of operational convection-allowing NWP. *Wea. Forecasting*, **23**, 931–952, https://doi.org/10.1175/WAF2007106.1.

Kalnay, E., 2002: *Atmospheric Modeling, Data Assimilation and Predictability*. Cambridge University Press, 341 pp.

Kleist, D. T., D. F. Parrish, J. C. Derber, R. Treadon, W.-S. Wu, and S. Lord, 2009: Introduction of the GSI into the NCEP Global Data Assimilation System. *Wea. Forecasting*, **24**, 1691–1705, https://doi.org/10.1175/2009WAF2222201.1.

Kong, R., M. Xue, and C. Liu, 2018: Development of a hybrid En3DVar data assimilation system and comparisons with 3DVar and EnKF for radar data assimilation with observing system simulation experiments. *Mon. Wea. Rev.*, **146**, 175–198, https://doi.org/10.1175/MWR-D-17-0164.1.

——, ——, A. O. Fierro, Y. Jung, C. Liu, E. R. Mansell, and D. R. MacGorman, 2020: Assimilation of GOES-R Geostationary Lightning Mapper flash extent density data in GSI EnKF for the analysis and short-term forecast of a mesoscale convective system. *Mon. Wea. Rev.*, **148**, 2111–2133, https://doi.org/10.1175/MWR-D-19-0192.1.

——, ——, C. S. Liu, and Y. Jung, 2021: Comparisons of hybrid En3DVar with 3DVar and EnKF for radar data assimilation: Tests with the 10 May 2010 Oklahoma tornado outbreak. *Mon. Wea. Rev.*, **149**, 21–40, https://doi.org/10.1175/MWR-D-20-0053.1.

——, ——, C. Liu, A. O. Fierro, and E. R. Mansell, 2022: Development of new observation operators for assimilating GOES-R Geostationary Lightning Mapper flash extent density data using GSI EnKF: Tests with two convective events over the United States. *Mon. Wea. Rev.*, **150**, 2091–2110, https://doi.org/10.1175/MWR-D-21-0326.1.

——, ——, E. R. Mansell, C. Liu, and A. O. Fierro, 2024: Assimilation of GOES-R Geostationary Lightning Mapper flash extent density data in GSI 3DVar, EnKF, and hybrid En3DVar for the analysis and short-term forecast of a supercell storm case. *Adv. Atmos. Sci.*, **41**, 263–277, https://doi.org/10.1007/s00376-023-2340-2.

Kotsuki, S., Y. Ota, and T. Miyoshi, 2017: Adaptive covariance relaxation methods for ensemble data assimilation: Experiments in the real atmosphere. *Quart. J. Roy. Meteor. Soc.*, **143**, 2001–2015, https://doi.org/10.1002/qj.3060.

Lei, L., J. S. Whitaker, and C. Bishop, 2018: Improving assimilation of radiance observations by implementing model space localization in an ensemble Kalman filter. *J. Adv. Model. Earth Syst.*, **10**, 3221–3232, https://doi.org/10.1029/2018MS001468.

Lin, S.-J., 2004: A "vertically Lagrangian" finite-volume dynamical core for global models. *Mon. Wea. Rev.*, **132**, 2293–2307, https://doi.org/10.1175/1520-0493(2004)132<2293:AVLFDC>2.0.CO;2.

Liu, C., Q. Xiao, and Bin. Wang, 2009: An ensemble-based four-dimensional variational data assimilation scheme. Part II: Observing system simulation experiments with Advanced Research WRF (ARW). *Mon. Wea. Rev.*, **137**, 1687–1704, https://doi.org/10.1175/2008MWR2699.1.

——, M. Xue, and R. Kong, 2019: Direct assimilation of radar reflectivity data using 3DVAR: Treatment of hydrometeor background errors and OSSE tests. *Mon. Wea. Rev.*, **147**, 17–29, https://doi.org/10.1175/MWR-D-18-0033.1.

——, ——, and ——, 2020: Direct variational assimilation of radar reflectivity and radial velocity data: Issues with nonlinear reflectivity operator and solutions. *Mon. Wea. Rev.*, **148**, 1483–1502, https://doi.org/10.1175/MWR-D-19-0149.1.

Liu, J., E. J. Fertig, H. Li, E. Kalnay, B. R. Hunt, E. J. Kostelich, I. Szunyogh, and R. Todling, 2008: Comparison between local ensemble transform Kalman filter and PSAS in the NASA finite volume GCM—Perfect model experiments. *Nonlinear Processes Geophys.*, **15**, 645–659, https://doi.org/10.5194/npg-15-645-2008.

Liu, Z., and Coauthors, 2022: Data assimilation for the Model for Prediction Across Scales–atmosphere with the Joint Effort for Data Assimilation Integration (JEDI-MPAS 1.0.0): EnVar implementation and evaluation. *Geosci. Model Dev.*, **15**, 7859–7878, https://doi.org/10.5194/gmd-15-7859-2022.

Lorenc, A. C., 2003: The potential of the ensemble Kalman filter for NWP—A comparison with 4D-Var. *Quart. J. Roy. Meteor. Soc.*, **129**, 3183–3203, https://doi.org/10.1256/qj.02.132.

Lorenz, E. N., 1956: Empirical orthogonal functions and statistical weather prediction. Statistical Forecasting Project Rep. 1, 52 pp., https://wind.mit.edu/~emanuel/Lorenz/EdLorenz/Empirical_Orthogonal_Functions_1956.pdf.

Maldonado, P., J. Ruiz, and C. Saulo, 2020: Parameter sensitivity of the WRF–LETKF system for assimilation of radar observations: Imperfect-model observing system simulation experiments. *Wea. Forecasting*, **35**, 1345–1362, https://doi.org/10.1175/WAF-D-19-0161.1.

Mansell, E. R., 2014: Storm-scale ensemble Kalman filter assimilation of total lightning flash-extent data. *Mon. Wea. Rev.*, **142**, 3683–3695, https://doi.org/10.1175/MWR-D-14-00061.1.

——, D. R. MacGorman, C. L. Ziegler, and J. M. Straka, 2002: Simulated three-dimensional branched lightning in a numerical thunderstorm model. *J. Geophys. Res.*, **107**, 4075, https://doi.org/10.1029/2000JD000244.

Mansell, E. R., C. L. Ziegler, and D. R. MacGorman, 2007: A lightning data assimilation technique for mesoscale forecast models. *Mon. Wea. Rev.*, **135**, 1732–1748, https://doi.org/10.1175/MWR3387.1.

Marchand, M. R., and H. E. Fuelberg, 2014: Assimilation of lightning data using a nudging method involving low-level warming. *Mon. Wea. Rev.*, **142**, 4850–4871, https://doi.org/10.1175/MWR-D-14-00076.1.

Ménétrier, B., 2020: Normalized interpolated convolution from an adaptive subgrid: Documentation. Accessed 6 May 2024, https://github.com/benjaminmenetrier/nicas_doc/blob/master/nicas_doc.pdf.

Minamide, M., and F. Zhang, 2018: Assimilation of all-sky infrared radiances from *Himawari-8* and impacts of moisture and hydrometer initialization on convection-permitting tropical cyclone prediction. *Mon. Wea. Rev.*, **146**, 3241–3258, https://doi.org/10.1175/MWR-D-17-0367.1.

Miyoshi, T., and S. Yamane, 2007: Local ensemble transform Kalman filtering with an AGCM at a T159/L48 resolution. *Mon. Wea. Rev.*, **135**, 3841–3861, https://doi.org/10.1175/2007MWR1873.1.

Mlawer, E. J., S. J. Taubman, P. D. Brown, M. J. Iacono, and S. A. Clough, 1997: Radiative transfer for inhomogeneous atmospheres: RRTM, a validated correlated-k model for the longwave. *J. Geophys. Res.*, **102**, 16 663–16 682, https://doi.org/10.1029/97JD00237.

Nakanishi, M., and H. Niino, 2009: Development of an improved turbulence closure model for the atmospheric boundary layer. *J. Meteor. Soc. Japan*, **87**, 895–912, https://doi.org/10.2151/jmsj.87.895.

Nerger, L., T. Janjic, J. Schroter, and W. Hiller, 2012: A regulated localization scheme for ensemble-based Kalman filters. *Quart. J. Roy. Meteor. Soc.*, **138**, 802–812, https://doi.org/10.1002/qj.945.

Niu, G.-Y., and Coauthors, 2011: The community Noah land surface model with multiparameterization options (Noah-MP): 1. Model description and evaluation with local-scale measurements. *J. Geophys. Res.*, **116**, D12109, https://doi.org/10.1029/2010JD015139.

Olson, J. B., J. S. Kenyon, W. A. Angevine, J. M. Brown, M. Pagowski, and K. Suselj, 2019: A description of the MYNN-EDMF scheme and the coupling to other components in WRF-ARW. NOAA Tech. Memo. OAR GSD-61, 42 pp., https://doi.org/10.25923/n9wm-be49.

Ott, E., and Coauthors, 2004: A local ensemble Kalman filter for atmospheric data assimilation. *Tellus*, **56A**, 415–428, https://doi.org/10.3402/tellusa.v56i5.14462.

Papadopoulos, A., T. G. Chronis, and E. N. Anagnostou, 2005: Improving convective precipitation forecasting through assimilation of regional lightning measurements in a mesoscale model. *Mon. Wea. Rev.*, **133**, 1961–1977, https://doi.org/10.1175/MWR2957.1.

Park, J., M. Xue, and C. Liu, 2023: Implementation and testing of radar data assimilation capabilities within the joint effort for data assimilation integration framework with ensemble transformation Kalman filter coupled with FV3-LAM model. *Geophys. Res. Lett.*, **50**, e2022GL102709, https://doi.org/10.1029/2022GL102709.

Putman, W. M., and S.-J. Lin, 2007: Finite-volume transport on various cubed-sphere grids. *J. Comput. Phys.*, **227**, 55–78, https://doi.org/10.1016/j.jcp.2007.07.022.

Roberts, N. M., and H. W. Lean, 2008: Scale-selective verification of rainfall accumulations from high-resolution forecasts of convective events. *Mon. Wea. Rev.*, **136**, 78–97, https://doi.org/10.1175/2007MWR2123.1.

Roebber, P. J., 2009: Visualizing multiple measures of forecast quality. *Wea. Forecasting*, **24**, 601–608, https://doi.org/10.1175/2008WAF2222159.1.

Sawada, Y., K. Okamoto, M. Kunii, and T. Miyoshi, 2019: Assimilating every-10-minute Himawari-8 infrared radiances to improve convective predictability. *J. Geophys. Res. Atmos.*, **124**, 2546–2561, https://doi.org/10.1029/2018JD029643.

Snyder, C., and F. Zhang, 2003: Assimilation of simulated Doppler radar observations with an ensemble Kalman filter. *Mon. Wea. Rev.*, **131**, 1663–1677, https://doi.org/10.1175//2555.1.

Sun, J., and N. A. Crook, 1997: Dynamical and microphysical retrieval from Doppler radar observations using a cloud model and its adjoint. Part I: Model development and simulated data experiments. *J. Atmos. Sci.*, **54**, 1642–1661, https://doi.org/10.1175/1520-0469(1997)054<1642:DAMRFD>2.0.CO;2.

——, and H. Wang, 2013: Radar data assimilation with WRF 4D-var. Part II: Comparison with 3D-var for a squall line over the U.S. Great Plains. *Mon. Wea. Rev.*, **141**, 2245–2264, https://doi.org/10.1175/MWR-D-12-00169.1.

Thompson, G., P. R. Field, R. M. Rasmussen, and W. D. Hall, 2008: Explicit forecasts of winter precipitation using an improved bulk microphysics scheme. Part II: Implementation of a new snow parameterization. *Mon. Wea. Rev.*, **136**, 5095–5115, https://doi.org/10.1175/2008MWR2387.1.

Tong, C.-C., M. Xue, C. Liu, J. Luo, and Y. Jung, 2024: Development of multiscale EnKF within GSI and its applications to multiple convective storm cases with radar reflectivity data assimilation using the FV3 limited-area model. *Mon. Wea Rev.*, **152**, 1839–1857, https://doi.org/10.1175/MWR-D-23-0235.1.

Tong, M., and M. Xue, 2005: Ensemble Kalman filter assimilation of Doppler radar data with a compressible nonhydrostatic model: OSS experiments. *Mon. Wea. Rev.*, **133**, 1789–1807, https://doi.org/10.1175/MWR2898.1.

Whitaker, J. S., and T. M. Hamill, 2012: Evaluating methods to account for system errors in ensemble data assimilation. *Mon. Wea. Rev.*, **140**, 3078–3089, https://doi.org/10.1175/MWR-D-11-00276.1.

——, ——, Xue. Wei, Y. Song, and Z. Toth, 2008: Ensemble data assimilation with the NCEP Global Forecast System. *Mon. Wea. Rev.*, **136**, 463–482, https://doi.org/10.1175/2007MWR2018.1.

Xiao, X., J. Sun, X. Qie, Z. Ying, L. Ji, M. Chen, and L. Zhang, 2021: Lightning data assimilation scheme in a 4DVAR system and its impact on very short-term convective forecasting. *Mon. Wea. Rev.*, **149**, 353–373, https://doi.org/10.1175/MWR-D-19-0396.1.

Xue, M., D. Wang, J. Gao, K. Brewster, and K. K. Droegemeier, 2003: The Advanced Regional Prediction System (ARPS), storm-scale numerical weather prediction and data assimilation. *Meteor. Atmos. Phys.*, **82**, 139–170, https://doi.org/10.1007/s00703-001-0595-6.

Zhang, F., M. Minamide, and E. E. Clothiaux, 2016a: Potential impacts of assimilating all-sky infrared satellite radiances from GOES-R on convection-permitting analysis and prediction of tropical cyclones. *Geophys. Res. Lett.*, **43**, 2954–2963, https://doi.org/10.1002/2016GL068468.

Zhang, F. Q., C. Snyder, and J. Sun, 2004: Impacts of initial estimate and observation availability on convective-scale data assimilation with an ensemble Kalman filter. *Mon. Wea. Rev.*, **132**, 1238–1253, https://doi.org/10.1175/1520-0493(2004)132<1238:IOIEAO>2.0.CO;2.

Zhang, J., and Coauthors, 2016b: Multi-Radar Multi-Sensor (MRMS) quantitative precipitation estimation: Initial operating capabilities. *Bull. Amer. Meteor. Soc.*, **97**, 621–638, https://doi.org/10.1175/BAMS-D-14-00174.1.

Zhang, Y., F. Zhang, and D. Stensrud, 2018: Assimilating all-sky infrared radiances from GOES-16 ABI using an ensemble Kalman filter for convection-allowing severe thunderstorms prediction. *Mon. Wea. Rev.*, **146**, 3363–3381, https://doi.org/10.1175/MWR-D-18-0062.1.

Zhu, L., M. Xue, R. Kong, and J. Min, 2023: Direct assimilation of all-sky GOES-R ABI radiances in GSI EnKF for the analysis and forecasting of a mesoscale convective system. *Mon. Wea. Rev.*, **151**, 737–760, https://doi.org/10.1175/MWR-D-21-0293.1.